

DyBluRF: Dynamic Deblurring Neural Radiance Fields for Blurry Monocular Video

Minh-Quan Viet Bui^{1*}, Jongmin Park^{1*}, Jihyong Oh^{2†}, and Munchurl Kim^{1†}

¹ KAIST, ² Chung-Ang University

{bvmquan, jm.park, mkimee}@kaist.ac.kr jihyongoh@cau.ac.kr

<https://kaist-viclab.github.io/dyblurf-site/>

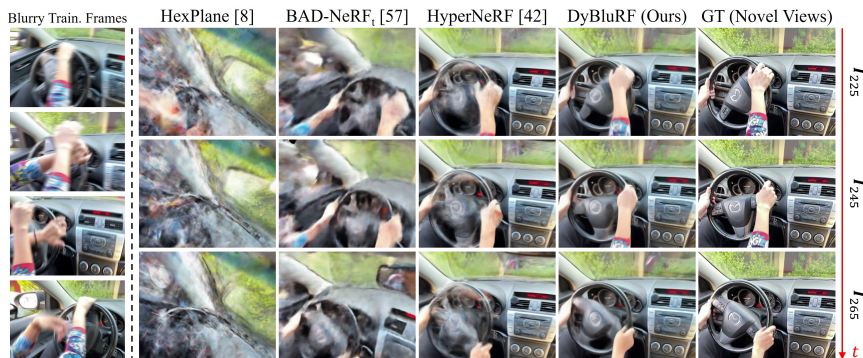


Fig. 1: Dynamic deblurring novel view synthesis. We *first* propose a novel dynamic deblurring NeRF for *blurry* monocular videos, called DyBluRF, which significantly outperforms previous SOTA NeRFs, trained our synthesized Blurry iPhone dataset.

Abstract. Neural Radiance Fields (NeRF), initially developed for static scenes, have inspired many video novel view synthesis techniques. However, the challenge for video view synthesis arises from motion blur, a consequence of object or camera movement during exposure, which hinders the precise synthesis of sharp spatio-temporal views. In response, we propose a novel dynamic deblurring NeRF framework for blurry monocular video, called DyBluRF, consisting of a Base Ray Initialization (BRI) stage and a Motion Decomposition-based Deblurring (MDD) stage. Our DyBluRF is the first that handles the novel view synthesis for blurry monocular video with a novel two-stage framework. In the BRI stage, we coarsely reconstruct dynamic 3D scenes and jointly initialize the base ray, which is further used to predict latent sharp rays, using the inaccurate camera pose information from the given blurry frames. In the MDD stage, we introduce a novel Incremental Latent Sharp-rays Prediction (ILSP) approach for the blurry monocular video frames by decomposing the latent sharp rays into global camera motion and local object motion components. We further propose two loss functions for effective geometry regularization and decomposition of static and dynamic scene components without any mask supervision. Experiments show that DyBluRF outperforms qualitatively and quantitatively the SOTA methods.

Keywords: Deblurring NeRF · Dynamic NeRF · Video View Synthesis

* Co-first authors (equal contribution), † Co-corresponding authors

1 Introduction

Free viewpoint rendering for spatio-temporal novel view synthesis has increased lots of interests due to its diverse applications. Especially, video view synthesis can render visually pleasing frames at arbitrary camera viewpoints and time instances. After the first advent of neural radiance fields for a static scene, called NeRF [33], diverse types of neural rendering methods [27, 45, 56, 60] for video view synthesis have actively been developed. Multi-view-based methods [7, 11, 27, 37, 69, 73] have been traditionally adopted for free viewpoint rendering of dynamic videos. However, they need a synchronized capturing process for multi-camera systems which are impractical for general users. To overcome this, several methods of dynamic view synthesis [4, 16, 18, 28, 29, 43, 48, 54] for a casually captured monocular video have been proposed for easier applications.

On the other hand, motion blur arises as a consequence of either object motion [39, 68] or camera shake [5, 67] caused by the accumulation of light during video acquisition [20, 21, 36, 53]. Therefore, synthesizing *sharp* novel spatio-temporal views from monocular video is faced with several challenges when *blurriness* presents in the given frames due to the camera capture process: (i) One straightforward solution is to apply 2D video deblurring [26, 40, 72] as a preprocessing step to the given blurry frames before optimizing video NeRFs. However, this naive approach has a significant drawback as independently deblurring frames in the pixel domain can introduce inconsistent geometry in 3D space [24, 25], which cannot be corrected through video NeRF optimization; (ii) Although several deblurring NeRFs [24, 25, 32, 57] have been developed to address blurriness in *static* multi-view images, they encounter difficulties in capturing temporal information when extended to blurry monocular videos. This is due to the absence of a motion-aware deblurring module along the temporal dimension. Additionally, the existing state-of-the-art (SOTA) monocular video NeRF methods [8, 15, 42, 62] cannot be directly applied to dynamic deblurring novel view synthesis from given blurry frames because they lack an effective deblurring component; (iii) Moreover, directly modeling the blur process using camera poses extracted from blurry monocular videos leads to inaccurate 3D geometry of the scene and compromised rendering quality [57].

To address these, we *first* propose a novel dynamic deblurring NeRF for blurry monocular video, called DyBluRF which *significantly* outperforms the various methods of static deblurring NeRFs [24, 32, 57], dynamic NeRFs [8, 15, 19, 42, 62], and the cascades of a 2D deblurring method [26] and dynamic NeRFs [19, 42, 62] (see Tab. 1). Our contributions are as follows:

- We *firstly* propose a novel dynamic deblurring NeRF framework, called DyBluRF, which can effectively render the sharp novel spatio-temporal views from blurry monocular videos.
- We propose a novel *Base Ray Initialization* (BRI) stage which simultaneously performs the reconstruction of dynamic 3D scenes and the initialization of base rays from the camera poses extracted from blurry video frames in an interleave manner;

- We propose a novel *Motion Decomposition-based Deblurring* (MDD) stage which includes a novel Incremental Latent Sharp-rays Prediction (ILSP) approach to effectively handle the blurriness due to global camera and local object motions in the monocular videos;
- We propose two simple yet effective loss functions: Unsupervised Staticness Maximization Loss \mathcal{L}_{sm} for effectively optimizing sharp radiance fields without any mask supervision, and Local Geometry Variance Distillation \mathcal{L}_{lg} for reconstructing robust geometry;
- For experiments, we synthesize a new blurry version of iPhone dataset [19] which is used to train the DyBluRF and other methods under fair comparison. The experimental results demonstrate that our DyBluRF achieves superior performances compared to previous SOTA methods, both qualitatively (Fig. 1) and quantitatively (Tab. 1), in dynamic deblurring for novel view synthesis, and it is robust against degrees of blurriness (Fig. 3, Tab. 2).

2 Related Work

2.1 Conventional Video Deblurring

Motion blur can be attributed to either objects in motion [39, 68] or camera shake [5, 67], both of which stem from the gathering of light during video capture over the exposure time [20, 21, 36, 53]. Various deep learning methods [12, 26, 30, 38, 58, 66, 71] have been developed for video deblurring. However, naively applying conventional video deblurring as a preprocessing step to the given blurry frames before optimizing video NeRFs induces inconsistent geometry in 3D space [24, 25], which cannot be corrected through video NeRF optimization.

2.2 Deblurring NeRFs for Static Scenes

To produce visually appealing frames with consistent 3D geometry from blurry multi-view *static* images, several NeRF [33]-based methods have emerged. DeblurNeRF [32] employs an end-to-end volume rendering framework [13] to estimate spatial blur kernels at the pixel level and the latent sharp radiance fields. BAD-NeRF [57] jointly predicts the virtual camera trajectories during the image exposure capture time. DP-NeRF [24] introduces a rigid blurring kernel to maintain 3D consistency by leveraging physical constraints. ExBluRF [25] introduces an MLP-based framework for reducing the dimensionality of 6-DOF camera poses and employing a voxel-based radiance field [9, 17]. Nonetheless, none of the above methods *can be applicable for non-rigid video view synthesis* due to the lack of motion-aware deblurring for the temporal dimension.

2.3 NeRFs for Dynamic Scenes

Recent methods for video view synthesis have expanded upon the static NeRF framework [33]. They represent dynamic NeRFs by incorporating scene flow-based frameworks [18, 28, 29] or canonical fields [3, 15, 22, 31, 41, 42, 45, 51, 54, 61, 65]

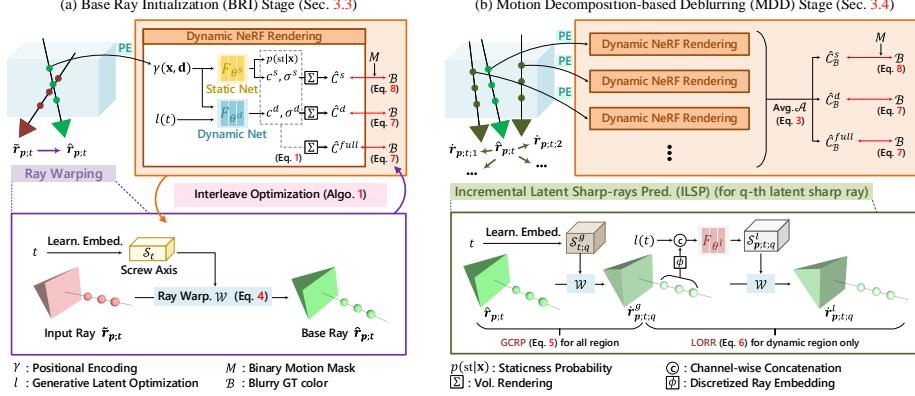


Fig. 2: Overview of our DyBluRF framework. To effectively optimize the sharp radiance field with the imprecise camera poses extracted from blurry video frames, we design our DyBluRF consisting of two main procedures (Algo. 2 in *Supplemental*) of (a) *Base Ray Initialization (BRI) Stage* (Sec. 3.3 and Algo. 1 in *Supplemental*) and (b) *Motion Decomposition-based Deblurring (MDD) Stage* (Sec. 3.4).

to model non-rigid deformable transformations or 4D spatio-temporal radiance fields [4, 8, 14, 16, 18, 27, 28, 48, 55, 63]. The methods such as NSFF [28], DynamicNeRF [18], and DynIBaR [29] typically combine two types of NeRFs: time-invariant and time-variant, to generate novel spatio-temporal views for monocular videos. However, they rely heavily on pretrained motion mask extraction for moving objects and various regularization losses for 3D scene flows, which makes them less effective in deblurring video view synthesis. The methods of T-NeRF [19], HyperNeRF [42], TiNeuVox [15], and 4D-GS [62] initially learn deformation or offset fields that transform a ray in an observation space to a bent ray in a canonical space. However, none of the above existing SOTA monocular video NeRF methods can be readily applied for deblurred neural radiance fields from the given blurry frames due to the lack of an effective deblurring strategy.

3 Proposed Method: DyBluRF

3.1 Design Considerations

Our DyBluRF is *firstly* designed to represent *sharp* dynamic neural radiance fields from *blurry* monocular videos, which consists of two main stages: Base Ray Initialization (BRI) and Motion Decomposition-based Deblurring (MDD), as shown in Fig. 2. We provide the detailed process of our DyBluRF with pseudocodes of two algorithms in *Supplemental*.

To reconstruct sharp dynamic radiance fields from blurry monocular videos, accurate prediction of latent sharp rays during exposure time is essential [24, 32, 57]. This process aims to render the values of blurry pixels in accordance with the physical process. Typically, latent sharp rays are estimated by calculating the residual transformation from a base ray [24]. However, if we directly utilize the input rays which are derived from the camera poses obtained through

Structure from Motion (SfM) algorithms [47] from blurry videos as the base rays, incorrect latent sharp rays [57] may be obtained. Moreover, in video view synthesis, jointly optimizing dynamic radiance fields and predicting latent sharp rays from imprecise base rays can lead to suboptimal solutions. To overcome these issues, distinguished from prior static deblur NeRFs [24, 32, 57] which directly predict latent rays from imprecise input cameras, we *newly* propose the BRI stage (Sec. 3.3) to provide a stronger foundation for the accurate prediction of latent sharp rays. The BRI stage coarsely reconstructs robust dynamic radiance fields and refines the initialization of base rays using imprecise input camera rays.

On the other hand, the existing SOTA deblurring NeRFs [24, 25, 32, 57] only consider multi-view *static* images so they encounter the difficulties in capturing temporal information when extended for blurry *monocular* videos due to the absence of a motion-aware deblurring module. Moreover, the existing SOTA methods for monocular video view synthesis [8, 15, 42, 62] are not capable of handling the input blurry frames due to the lack of deblurring components. To overcome these limitations, we *newly* introduce the MDD stage (Sec. 3.4), with a novel Incremental Latent Sharp-rays Prediction (ILSP) method which can effectively synthesize the physical blur process considering global camera and local object motions in a progressive manner along temporal axis.

3.2 Preliminaries

Dynamic Neural Radiance Fields. We extend the static NeRF [33] to our DyBluRF for the monocular video which consists of one frame per time t . Our DyBluRF learns to represent the continuous radiance of a video scene using neural networks, taking into account a set of N_f frames from the monocular video, denoted as $\{\mathcal{I}_t\}_{t=1}^{N_f}$, and the corresponding camera poses $\{\mathcal{P}_t\}_{t=1}^{N_f}$. Following [18, 28, 29, 31], we decompose our radiance representation into Static Net F_{θ^s} and Dynamic Net F_{θ^d} . Given a 3D position $\mathbf{x} = (x, y, z)$ and a viewing direction \mathbf{d} , $F_{\theta^s} : \gamma(\mathbf{x}, \mathbf{d}) \rightarrow (\mathbf{c}^s, \sigma^s, p(\text{st}|\mathbf{x}))$ estimates a color \mathbf{c}^s , a volume density σ^s of static scene component and a staticness probability $p(\text{st}|\mathbf{x})$ which indicates that \mathbf{x} is static from the spatial positional encoded inputs $\gamma(\mathbf{x}, \mathbf{d})$. On the other hand, $F_{\theta^d} : (\gamma(\mathbf{x}, \mathbf{d}), l(t)) \rightarrow (\mathbf{c}^d, \sigma^d)$ maps a time-varying embedding to a color \mathbf{c}^d and a volume density σ^d of dynamic scene component where γ is the positional encoding [33] and l is Generative Latent Optimization (GLO) [6]. Let $\mathbf{r}_{\mathbf{p};t}(s) = \mathbf{o}_t + s\mathbf{d}_{\mathbf{p};t}$ be the cast ray from a camera origin \mathbf{o}_t through a given pixel \mathbf{p} of the image plane at the time t where s and $\mathbf{d}_{\mathbf{p};t}$ denote a sampling ray distance and a viewing direction through the pixel \mathbf{p} at time t , respectively. We separately estimate the rendered colors $\hat{\mathbf{C}}^s(\mathbf{r}_{\mathbf{p};t})$ of the static scene component and $\hat{\mathbf{C}}^d(\mathbf{r}_{\mathbf{p};t})$ of the dynamic scene component via continuous volume rendering [13] by computing the integral on N piecewise constant segments $\{[s_n, s_{n+1}]\}_{n=1}^N$ along the ray $\mathbf{r}_{\mathbf{p};t}$ as $\hat{\mathbf{C}}^s(\mathbf{r}_{\mathbf{p};t}) = \sum_{n=1}^N \mathcal{T}_n^s \alpha_n^s \mathbf{c}_n^s$ and $\hat{\mathbf{C}}^d(\mathbf{r}_{\mathbf{p};t}) = \sum_{n=1}^N \mathcal{T}_n^d \alpha_n^d \mathbf{c}_n^d$ where \mathcal{T}_n is the accumulated transmittance and α_n is the alpha-compositing weight. Here, $\alpha_n = 1 - \exp(-\sigma_n \delta_n)$ and $\mathcal{T}_n = \prod_{k=1}^{n-1} 1 - \alpha_k$ where $\delta_n = s_{n+1} - s_n$ is the segment length. To predict the full rendered color $\hat{\mathbf{C}}^{full}(\mathbf{r}_{\mathbf{p};t})$ of the pixel \mathbf{p} with

\mathcal{P}_t , our DyBluRF combines the outputs of F_{θ^s} and F_{θ^d} via the probabilistic volume rendering as:

$$\hat{\mathcal{C}}^{full}(\mathbf{r}_{\mathbf{p};t}) = \sum_{n=1}^N \mathcal{T}_n^{full} \left(p(\text{st}|\mathbf{x}_n) \alpha_n^s \mathbf{c}_n^s + (1 - p(\text{st}|\mathbf{x}_n)) \alpha_n^d \mathbf{c}_n^d \right), \quad (1)$$

where \mathbf{x}_n is the n^{th} 3D point and the full accumulated transmittance \mathcal{T}_n^{full} equals $\prod_{k=1}^{n-1} (1 - p(\text{st}|\mathbf{x}_k) \alpha_k^s) (1 - (1 - p(\text{st}|\mathbf{x}_k) \alpha_k^d))$.

Binary Motion Mask Prediction. Learning the motion decomposition has been widely adopted in previous works [18, 27, 29] to stabilize the reconstruction of static scene components in the dynamic NeRFs. In our DyBluRF, we also predict the 2D binary motion mask for the BRI stage and the MDD stage optimizations. The binary motion mask $\mathbf{M}(\mathbf{r}_{\mathbf{p};t})$ can be obtained by thresholding the dynamicness probability $p(\text{dy}|\mathbf{r}_{\mathbf{p};t}) > 0.5$, where $p(\text{dy}|\mathbf{r}_{\mathbf{p};t})$ is the accumulated dynamicness probability of all sampling points \mathbf{x}_n along $\mathbf{r}_{\mathbf{p};t}$ as:

$$p(\text{dy}|\mathbf{r}_{\mathbf{p};t}) = \sum_{\mathbf{x}_n} p(\mathbf{x}_n|\mathbf{r}_{\mathbf{p};t}) p(\text{dy}|\mathbf{x}_n, \mathbf{r}_{\mathbf{p};t}) = \sum_{\mathbf{x}_n} p(\mathbf{x}_n|\mathbf{r}_{\mathbf{p};t}) (1 - p(\text{st}|\mathbf{x}_n, \mathbf{r}_{\mathbf{p};t})), \quad (2)$$

where we assume that $p(\text{st}|\mathbf{x}_n, \mathbf{r}_{\mathbf{p};t})$ is equal to $p(\text{st}|\mathbf{x}_n)$, as the staticness probability of the 3D sampling point \mathbf{x}_n should remain consistent regardless of the cast ray and the time index. Thus, using $p(\text{st}|\mathbf{x})$ from F_{θ^s} suffices to estimate the binary motion mask. The probability $p(\mathbf{x}_n|\mathbf{r}_{\mathbf{p};t})$ is computed from accumulated transmittance and alpha-compositing weight.

Deblurring Neural Radiance Fields. To solve the blur problem for reconstructing sharp radiance fields, we predict the pixel-wise blur kernels and sharp pixel colors to simulate the physical blur process similar to the existing deblurring static NeRF methods [24, 32, 57]. The physical blur process which generates a blurry color $\mathcal{B}_{\mathbf{p};t}$ of pixel \mathbf{p} at time t by applying an unknown *motion* blur kernel $k_{\mathbf{p};t}$ along the spatio-temporal direction to the set of sharp pixel colors $\mathcal{I}_{\mathbf{p};t}$ is formulated as $\mathcal{B}_{\mathbf{p};t} = k_{\mathbf{p};t} * \mathcal{I}_{\mathbf{p};t}$ where $*$ indicates the spatio-temporal convolution operation [34–36, 49, 57]. We train our DyBluRF with the given blurry monocular video frames $\{\mathcal{B}_t\}_{t=1}^{N_f}$ with inaccurate camera poses $\{\tilde{\mathcal{P}}_t\}_{t=1}^{N_f}$. To optimize our DyBluRF using the blurry frames, we model the blur process for monocular dynamic radiance fields by predicting the set of latent sharp rays $\{\dot{\mathbf{r}}_{\mathbf{p};t;q}\}_{q=1}^{N_b}$ casting based on the ray $\mathbf{r}_{\mathbf{p};t}$ that we refer to as the *base ray*. Then, we average the corresponding volume rendered pixel colors to generate a blurry pixel color where q is the index and N_b is the number of latent sharp rays, respectively. We denote this motion blur process as:

$$\hat{\mathcal{C}}_{\mathcal{B}}(\mathbf{r}_{\mathbf{p};t}) = \mathcal{A}(\hat{\mathcal{C}}(\mathbf{r}_{\mathbf{p};t}), \{\hat{\mathcal{C}}(\dot{\mathbf{r}}_{\mathbf{p};t;q})\}_{q=1}^{N_b}) = \frac{1}{N_b + 1} \left(\hat{\mathcal{C}}(\mathbf{r}_{\mathbf{p};t}) + \sum_{q=1}^{N_b} \hat{\mathcal{C}}(\dot{\mathbf{r}}_{\mathbf{p};t;q}) \right), \quad (3)$$

where $\hat{\mathcal{C}}_{\mathcal{B}}(\mathbf{r}_{\mathbf{p};t})$ is a blurry rendered color of the base ray $\mathbf{r}_{\mathbf{p};t}$ and $\mathcal{A}(\cdot, \cdot)$ is an average function of the sharp rendered color $\hat{\mathcal{C}}(\mathbf{r}_{\mathbf{p};t})$ of $\mathbf{r}_{\mathbf{p};t}$ and the set of rendered colors $\{\hat{\mathcal{C}}(\dot{\mathbf{r}}_{\mathbf{p};t;q})\}_{q=1}^{N_b}$ of the corresponding latent sharp rays $\{\dot{\mathbf{r}}_{\mathbf{p};t;q}\}_{q=1}^{N_b}$.

3.3 Base Ray Initialization Stage

In the BRI stage, we initialize the base rays to predict accurate latent sharp rays by warping them from the input rays. This initialization is jointly trained with F_{θ^s} and F_{θ^d} via our proposed interleave optimization strategy, as shown in Fig. 2-(a). We detail our ray warping and interleave optimization.

Ray Warping. Let $\tilde{\mathbf{r}}_{\mathbf{p};t}$ represent an input ray emitted from pixel \mathbf{p} with a camera pose $\tilde{\mathcal{P}}_t$ from the blurry input video frame at time t . We initialize the base ray $\hat{\mathbf{r}}_{\mathbf{p};t}$ from the input ray $\tilde{\mathbf{r}}_{\mathbf{p};t}$ using a ray warping \mathcal{W} as:

$$\hat{\mathbf{r}}_{\mathbf{p};t} = \mathcal{W}(\tilde{\mathbf{r}}_{\mathbf{p};t}, \mathcal{S}_t) = e^{[\boldsymbol{\omega}_t]_{\times}} \tilde{\mathbf{r}}_{\mathbf{p};t} + \mathbf{G}_t \mathbf{v}_t, \quad (4)$$

where $\mathcal{S}_t = (\boldsymbol{\omega}_t; \mathbf{v}_t) \in \mathbb{R}^6$ is a learnable screw axis with the corresponding rotation encoding $\boldsymbol{\omega}_t \in \mathfrak{so}(3)$ and translation encoding \mathbf{v}_t at time t . The initialized base ray $\hat{\mathbf{r}}_{\mathbf{p};t}$ is specifically used as the term $\mathbf{r}_{\mathbf{p};t}$ in Eq. (3). Similar to the existing methods [24, 41], we compute the residual rotation $e^{[\boldsymbol{\omega}_t]_{\times}} = \mathbf{I} + \frac{\sin \theta}{\theta} [\boldsymbol{\omega}_t]_{\times} + \frac{1 - \cos \theta}{\theta^2} [\boldsymbol{\omega}_t]_{\times}^2$ and translation matrix $\mathbf{G}_t = \mathbf{I} + \frac{1 - \cos \theta}{\theta^2} [\boldsymbol{\omega}_t]_{\times} + \frac{\theta - \sin \theta}{\theta^3} [\boldsymbol{\omega}_t]_{\times}^2$, where $[\mathbf{w}]_{\times}$ is the cross-product matrix of vector \mathbf{w} and $\theta = \|\boldsymbol{\omega}_t\|$ is rotation angle at time t . We model \mathcal{S}_t as a learnable embedding of time t , as in Fig. 2-(a).

Interleave Optimization. As discussed in Sec. 3.1, jointly optimizing F_{θ^d} and base ray initialization is highly ill-posed and can lead to undesirable local minima. This issue arises because F_{θ^d} is prone to misinterpreting geometric inconsistencies, stemming from inaccurate base rays, as deformations of dynamic objects across time instances. This misinterpretation leads to unnecessary deformations of F_{θ^d} and additional errors in predicting latent sharp rays. To address this, we propose a novel interleave optimization strategy that alternates between optimizing the screw axis \mathcal{S}_t for ray warping and F_{θ^d} , as shown in Fig. 2-(a) and Algo. 1 in the *Supplemental* section. More specifically, for *even* iteration indices, we jointly update F_{θ^s} and the screw axis \mathcal{S}_t using the static geometry cues extracted by our 2D binary motion mask $\mathcal{M}(\hat{\mathbf{r}}_{\mathbf{p};t})$. For *odd* iteration indices, we update both F_{θ^s} and F_{θ^d} and keep the \mathcal{S}_t unchanged. This approach enhances the training stability by simultaneously advancing the learning of 3D dynamic reconstruction and initializing the base rays for deblurring in the MDD stage.

3.4 Motion Decomposition-based Deblurring Stage

In the MDD stage, we *first* propose a novel Incremental Latent Sharp-rays Prediction (ILSP) approach for the *blurry monocular video frames* as shown in Fig. 2-(b) combined with Algo. 1 in *Supplemental*, which is fully described in Algo. 2 in *Supplemental*. This approach comprises a global camera-motion-aware ray prediction and a local object-motion-aware ray refinement.

Global Camera-motion-aware Ray Prediction (GCRP). To model the camera motion blur process which occurs in both static and dynamic scene components, we estimate multiple latent sharp rays $\{\hat{\mathbf{r}}_{\mathbf{p};t;q}^g\}_{q=1}^{N_b}$ (Fig. 2-(b)) based on the initialized base ray $\hat{\mathbf{r}}_{\mathbf{p};t}$ (Eq. (4) and Fig. 2-(a)) as:

$$\{\hat{\mathbf{r}}_{\mathbf{p};t;q}^g\}_{q=1}^{N_b} = \{\mathcal{W}(\hat{\mathbf{r}}_{\mathbf{p};t}, \mathcal{S}_{t;q}^g)\}_{q=1}^{N_b}, \quad (5)$$

where \mathcal{W} is defined in Eq. (4) and $\mathcal{S}_{t;q}^g$ is a global camera-motion-aware screw axis which is a learnable embedding of t for the q^{th} latent sharp ray $\hat{\mathbf{r}}_{\mathbf{p};t;q}^g$. The global camera-motion-aware ray prediction (GCRP) maps the base ray $\hat{\mathbf{r}}_{\mathbf{p};t}$ that is the output of the BRI stage to N_b predicted latent sharp rays $\{\hat{\mathbf{r}}_{\mathbf{p};t;q}^g\}_{q=1}^{N_b}$ considering the global camera motion (one-to- N_b mapping).

Local Object-motion-aware Ray Refinement (LORR). If only a single motion-aware ray prediction, i.e., GCRP, is adopted for estimating latent sharp rays, the model tends to learn the outer mixture of diverse motions, combining global camera and local object motions. This may result in unnatural artifacts such as afterimage spread over the blurry training frames. To delicately handle detailed motions, we further decompose the blurry rays into local object motions along with the global camera motion by refining the q^{th} predicted latent sharp ray $\hat{\mathbf{r}}_{\mathbf{p};t;q}^g$ considering pixel-wise local object motion as:

$$\hat{\mathbf{r}}_{\mathbf{p};t;q}^l = \mathcal{W}(\hat{\mathbf{r}}_{\mathbf{p};t;q}^g, \mathcal{S}_{\mathbf{p};t;q}^l), \quad (6)$$

where $\mathcal{S}_{\mathbf{p};t;q}^l = F_{\theta^l}(\lceil \phi(\hat{\mathbf{r}}_{\mathbf{p};t;q}^g), l(t) \rceil)$ is a local object-motion-aware screw axis learned by a local object-motion MLP F_{θ^l} which takes a discretized ray embedding $\phi(\hat{\mathbf{r}}_{\mathbf{p};t;q}^g)$ [44] and the encoded time $l(t)$ as inputs. $\lceil \cdot \rceil$ refers to channel-wise concatenation. The local object-motion-aware ray refinement (LORR) maps each predicted latent sharp ray $\hat{\mathbf{r}}_{\mathbf{p};t;q}^g$ to a single corresponding refined latent sharp ray $\hat{\mathbf{r}}_{\mathbf{p};t;q}^l$ considering the local object motion (one-to-one mapping). Specifically, the LORR is only applied to the dynamic scene components which are indicated by the binary motion mask $\mathbf{M}(\hat{\mathbf{r}}_{\mathbf{p};t}) (=1)$.

To obtain the blurry color $\hat{\mathbf{C}}_{\mathcal{B}}$, we apply Eq. (3) to predicted latent sharp rays from Eq. (5) for the static scene components or from Eq. (6) for the dynamic scene components. This motion blur process is only applied only during the training stage. Please note that in the inference stage, the full color $\hat{\mathbf{C}}^{\text{full}}(\mathbf{r}_{\mathbf{p};t}^{\text{inf}})$ of the inference target ray $\mathbf{r}_{\mathbf{p};t}^{\text{inf}}$ is synthesized for sharp target novel view.

3.5 Loss Function

We use diverse loss functions to effectively train DyBluRF as follows.

Photometric Loss. We minimize the L2 loss between the rendered color $\hat{\mathbf{C}}(\hat{\mathbf{r}}_{\mathbf{p};t})$ with the blurry GT color $\mathcal{B}_{\mathbf{p};t}$ as:

$$\mathcal{L}_{\text{photo}}(\hat{\mathbf{C}}(\hat{\mathbf{r}}_{\mathbf{p};t})) = \sum_{\hat{\mathbf{r}}_{\mathbf{p};t}} \|\hat{\mathbf{C}}(\hat{\mathbf{r}}_{\mathbf{p};t}) - \mathcal{B}_{\mathbf{p};t}\|_2^2, \quad (7)$$

where $\hat{\mathbf{C}}(\hat{\mathbf{r}}_{\mathbf{p};t})$ can be the rendered color of dynamic or full scene component $\hat{\mathbf{C}}^{\text{d,full}}(\hat{\mathbf{r}}_{\mathbf{p};t})$ in the BRI stage and the blurry rendered color $\hat{\mathbf{C}}_{\mathcal{B}}^{\text{d,full}}(\hat{\mathbf{r}}_{\mathbf{p};t})$ in the MDD stage. For the rendered color of static scene component $\hat{\mathbf{C}}^{\text{s}}(\hat{\mathbf{r}}_{\mathbf{p};t})$ in the BRI stage and $\hat{\mathbf{C}}_{\mathcal{B}}^{\text{s}}(\hat{\mathbf{r}}_{\mathbf{p};t})$ in the MDD stage, we adopt a masked photometric loss to prevent learning the dynamic scene component by using $\mathbf{M}(\hat{\mathbf{r}}_{\mathbf{p};t})$ as:

$$\mathcal{L}_{\text{mphoto}}(\hat{\mathbf{C}}(\hat{\mathbf{r}}_{\mathbf{p};t})) = \sum_{\hat{\mathbf{r}}_{\mathbf{p};t}} \|(\hat{\mathbf{C}}(\hat{\mathbf{r}}_{\mathbf{p};t}) - \mathcal{B}_{\mathbf{p};t}) \cdot (1 - \mathbf{M}(\hat{\mathbf{r}}_{\mathbf{p};t}))\|_2^2. \quad (8)$$

Unsupervised Staticness Maximization Loss (\mathcal{L}_{sm}). We observe that without any regularization for decomposition, F_{θ^s} and F_{θ^d} exhibit different convergence speeds, due to multi-view inconsistency for dynamic objects across time instances in F_{θ^s} which lacks any time modeling. As a result, F_{θ^d} quickly surpasses F_{θ^s} from the early stage, causing F_{θ^s} to degenerate and the staticness probability $p(\text{st}|\mathbf{x})$ to be all 0. Furthermore, the existing dynamic NeRFs [18, 28, 29, 31, 64] often rely on off-the-shelf models to obtain the moving object masks for the supervision of decomposition. To overcome these drawbacks, our DyBluRF is designed to predict the decomposition probability $p(\text{st}|\mathbf{x})$ and the binary motion mask $\mathbf{M}(\hat{\mathbf{r}}_{\mathbf{p};t})$ in an *unsupervised* manner. Specifically, we *newly* introduce a simple but effective loss function as an Unsupervised Staticness Maximization loss. We minimize the L1 loss of the logarithm of $p(\text{st}|\mathbf{x})$ weighted by λ_{sm} as $\mathcal{L}_{sm} = \lambda_{sm} \sum_{\mathbf{r}_{\mathbf{p};t}} |\log(p(\text{st}|\mathbf{x}))|$ to encourage the staticness probability $p(\text{st}|\mathbf{x})$ to preserve static characteristics, which can lead to robust decomposition.

Local Geometry Variance Distillation (\mathcal{L}_{lg}). Previous prior monocular dynamic NeRFs [28, 29, 31] commonly incorporate 2D monocular depth estimators [46] to regularize the geometry of radiance fields. However, as the monocular depths are scale- and shift-ambiguity, it is harmful to directly supervise them to learn the scene geometry. NSFF [28] and RoDynRF [31] proposed to normalize the GT depths and the NeRF’s depths extracted from the density fields for a scale- and shift-invariant supervision loss. DynIBaR [29] points out the instability of scale-invariant depth loss above and proposes to obtain scale-consistent depth maps by preprocessing the video sequence with [70]. However, the consistent depth preprocessing is much slower than 2D monocular depth estimation for long video sequences due to the time-consuming optical flow prediction [52] and exhausted keypoints matching. To overcome the above limitations, we propose a novel Local Geometry Variance Distillation to robustly regularize the density field of our F_{θ^d} with scale-ambiguity monocular depths. Specifically, using first-order finite differences, we approximate the gradients of 3D unprojection corresponding to the local kernel of the current pixel $\mathbf{p} = (p_u, p_v)$. Then, we compute the unit vector from the cross-product of the approximated partial derivatives of geometry to represent the local geometry variance at \mathbf{p} . The predicted $\hat{\mathbf{g}}_{\mathbf{p};t}$ and GT local geometry variance $\mathbf{g}_{\mathbf{p};t}$ are computed as:

$$\hat{\mathbf{g}}_{\mathbf{p};t} = \overline{\left(\frac{\partial \hat{\mathbf{r}}_{\mathbf{p};t}(s^*)}{\partial p_u} \times \frac{\partial \hat{\mathbf{r}}_{\mathbf{p};t}(s^*)}{\partial p_v} \right)}, \quad \mathbf{g}_{\mathbf{p};t} = \overline{\left(\frac{\partial \hat{\mathbf{r}}_{\mathbf{p};t}(\mathcal{D}_{\mathbf{p};t})}{\partial p_u} \times \frac{\partial \hat{\mathbf{r}}_{\mathbf{p};t}(\mathcal{D}_{\mathbf{p};t})}{\partial p_v} \right)}, \quad (9)$$

where $\overline{(\mathbf{w})}$ is the normalization operation of a vector \mathbf{w} and $s^* = \sum_{n=1}^N \mathcal{T}_n^d \alpha_n^d s_n^d$ is the volume rendered ray distance for the base ray $\hat{\mathbf{r}}_{\mathbf{p};t}$ and $\mathcal{D}_{\mathbf{p};t}$ is the corresponding scale-ambiguity depth values from DPT [46]. Our local geometry variance distillation is the L2 loss of $\hat{\mathbf{g}}_{\mathbf{p};t}$ and $\mathbf{g}_{\mathbf{p};t}$ weighted by a constant λ_{lg} as:

$$\mathcal{L}_{lg} = \lambda_{lg} \sum \|\hat{\mathbf{g}}_{\mathbf{p};t} - \mathbf{g}_{\mathbf{p};t}\|_2^2 \quad (10)$$

The gradient operation removes the shift-ambiguity and cross-product normalization removes the scale-ambiguity of $\mathcal{D}_{\mathbf{p};t}$. Hence, we can regularize the geometry with monocular depths regardless of both the scale- and shift-ambiguity.

4 Experiments

Implementation Details. We refer readers to the *Supplemental* for the details of our implementation.

Blurry iPhone Dataset. To assess the capabilities of our DyBluRF in deblurring dynamic novel view synthesis, we synthesize a new blurry version of iPhone dataset [19], called Blurry iPhone dataset. This dataset consists of synthetic blurry video frames $\{\mathcal{B}_t\}_{t=1}^{N_f}$ along with corresponding inaccurate camera poses $\{\mathcal{P}_t\}_{t=1}^{N_f}$ for training, and includes the original video frames and camera poses of the iPhone dataset [19] for evaluation. To synthesize realistic and natural blur during the camera exposure in the training video frames, we follow the approach of representative synthesized 2D video deblurring datasets [34, 35]. We utilize a Video Frame Interpolation (VFI) technique [50] to increase the frame rate of the iPhone dataset [19] from 30fps to virtual 240fps. Subsequently, we average these frames to generate virtual 30fps blurry video frames. Accompanying each blurry frame in the training dataset, we also synthesize inaccurate camera poses by simulating a smooth camera trajectory in 3D space [2, 23]. We provide more details of this synthesis process, along with figures, in *Supplemental*.

Metrics. To evaluate our DyBluRF and compare it with other SOTA methods in the monocular video settings, we utilize the co-visibility masked image metrics, including mPSNR, mSSIM, and mLPIPs, following the approach introduced by Dycheck [19]. These metrics mask out the regions of the test video frames which are not observed by the training camera. We further utilize tOF [10] to measure the temporal consistency of reconstructed video frames.

Table 1: Dynamic deblurring novel view synthesis evaluation on Blurry iPhone dataset. **Red** and **blue** denote the best and second best performances, respectively. Each block element of 4-performance denotes (mPSNR \uparrow / mSSIM \uparrow / mLPIPs \downarrow / tOF \downarrow). We also provide the complexity comparison in *Supplemental*.

Method	Apple	Block	Paper-windmill	Space-out
TiNeuVox [15]	13.53 / 0.680 / 0.723 / 1.704	10.79 / 0.558 / 0.676 / 1.705	14.15 / 0.273 / 0.781 / 4.108	14.18 / 0.557 / 0.587 / 1.385
HexPlane [8]	16.80 / 0.715 / 0.523 / 1.239	15.58 / 0.604 / 0.459 / 0.820	17.11 / 0.352 / 0.422 / 0.318	14.73 / 0.558 / 0.511 / 1.270
T-NeRF [19]	17.34 / 0.720 / 0.547 / 0.620	16.48 / 0.644 / 0.411 / 0.795	16.83 / 0.338 / 0.424 / 0.569	16.23 / 0.561 / 0.436 / 1.329
HyperNeRF [42]	14.31 / 0.681 / 0.663 / 1.411	16.12 / 0.642 / 0.416 / 0.958	16.59 / 0.335 / 0.365 / 0.666	17.79 / 0.631 / 0.332 / 0.402
4D-GS [62]	14.71 / 0.680 / 0.626 / 1.105	12.19 / 0.523 / 0.619 / 1.243	14.45 / 0.226 / 0.484 / 0.546	14.91 / 0.533 / 0.427 / 0.397
DP-NeRF _t [24]	11.97 / 0.665 / 0.717 / 2.072	9.96 / 0.514 / 0.729 / 1.602	12.66 / 0.241 / 0.713 / 1.482	13.15 / 0.532 / 0.628 / 0.639
BAD-NeRF _t [57]	12.29 / 0.668 / 0.744 / 1.743	9.61 / 0.517 / 0.736 / 1.290	12.44 / 0.266 / 0.564 / 0.973	12.57 / 0.508 / 0.643 / 0.437
GShiftNet [26] + [19]	16.83 / 0.719 / 0.532 / 0.666	16.32 / 0.641 / 0.403 / 0.839	16.65 / 0.323 / 0.369 / 0.476	17.75 / 0.617 / 0.347 / 0.455
GShiftNet [26] + [42]	14.31 / 0.676 / 0.622 / 1.332	15.71 / 0.626 / 0.417 / 0.942	16.31 / 0.328 / 0.310 / 0.566	17.52 / 0.618 / 0.296 / 0.555
GShiftNet [26] + [62]	14.62 / 0.674 / 0.619 / 1.111	12.46 / 0.525 / 0.623 / 0.950	14.35 / 0.214 / 0.468 / 0.643	14.71 / 0.524 / 0.401 / 0.412
DyBluRF (Ours)	18.03 / 0.737 / 0.505 / 0.479	17.35 / 0.660 / 0.361 / 0.735	18.08 / 0.413 / 0.282 / 0.238	18.83 / 0.644 / 0.314 / 0.264
Method	Spin	Teddy	Wheel	Average
TiNeuVox [15]	11.13 / 0.411 / 0.726 / 2.239	10.28 / 0.496 / 0.834 / 1.304	9.48 / 0.312 / 0.717 / 3.556	11.93 / 0.470 / 0.721 / 2.286
HexPlane [8]	16.02 / 0.482 / 0.563 / 1.253	12.84 / 0.497 / 0.587 / 1.220	12.87 / 0.409 / 0.521 / 1.336	15.14 / 0.517 / 0.512 / 1.065
T-NeRF [19]	17.16 / 0.503 / 0.534 / 1.162	14.07 / 0.562 / 0.464 / 1.094	14.93 / 0.499 / 0.379 / 1.360	16.15 / 0.547 / 0.456 / 0.990
HyperNeRF [42]	16.39 / 0.498 / 0.499 / 1.277	13.77 / 0.567 / 0.420 / 1.143	12.11 / 0.393 / 0.435 / 1.739	15.30 / 0.535 / 0.447 / 1.085
4D-GS [62]	14.31 / 0.418 / 0.513 / 1.522	12.18 / 0.492 / 0.564 / 1.402	10.44 / 0.309 / 0.583 / 2.004	13.31 / 0.455 / 0.545 / 1.174
DP-NeRF _t [24]	10.65 / 0.404 / 0.730 / 1.956	10.40 / 0.480 / 0.760 / 1.482	9.26 / 0.299 / 0.736 / 2.561	11.15 / 0.448 / 0.716 / 1.685
BAD-NeRF _t [57]	10.59 / 0.404 / 0.741 / 1.722	9.77 / 0.457 / 0.758 / 1.537	9.23 / 0.303 / 0.748 / 2.544	10.93 / 0.446 / 0.705 / 1.464
GShiftNet [26] + [19]	16.78 / 0.494 / 0.529 / 1.276	13.74 / 0.552 / 0.461 / 1.271	15.48 / 0.537 / 0.310 / 1.442	16.22 / 0.555 / 0.422 / 0.918
GShiftNet [26] + [42]	15.74 / 0.488 / 0.476 / 1.488	13.66 / 0.566 / 0.423 / 1.268	10.96 / 0.347 / 0.456 / 2.114	14.89 / 0.521 / 0.382 / 1.181
GShiftNet [26] + [62]	14.46 / 0.411 / 0.502 / 1.572	12.13 / 0.500 / 0.547 / 1.343	10.29 / 0.306 / 0.577 / 1.954	13.29 / 0.450 / 0.534 / 1.141
DyBluRF (Ours)	18.20 / 0.534 / 0.415 / 1.011	14.61 / 0.569 / 0.451 / 0.855	16.17 / 0.579 / 0.304 / 1.142	17.33 / 0.591 / 0.376 / 0.675

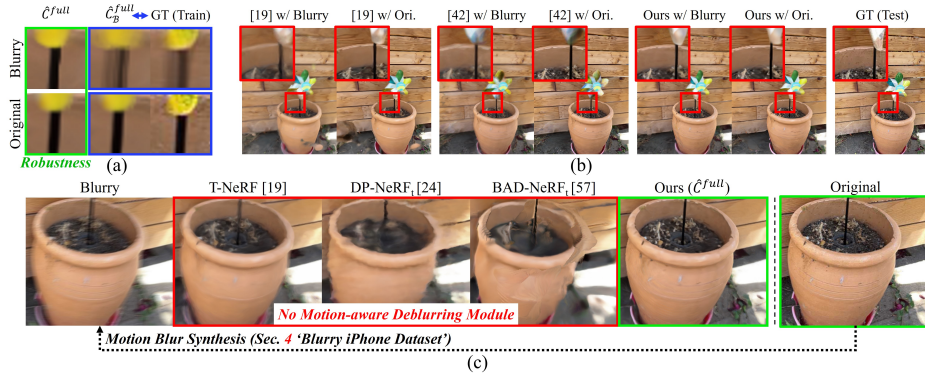


Fig. 3: Robustness of DyBluRF against degrees of blurriness. (a) \hat{C}^{full} , and \hat{C}_B^{full} refers to the rendering of the base rays and the averaged rendering computed with Eq. (3), respectively, by our DyBluRF. (b) ‘w/ Blurry’ and ‘w/ Ori.’ refer to the synthesized novel views by each method when trained with the Blurry iPhone dataset or the original iPhone dataset [19], respectively. (c) Comparisons given the original [19]’s poses. ‘Ours (\hat{C}^{full})’ refers to the sharp rendering by our DyBluRF trained with blurry frames (‘Blurry’), which appears similar to the corresponding original training frames (‘Original’), whereas other methods [19, 24, 57] fail to learn the sharp radiance fields from the blurry frames.

4.1 Experimental Results

In our experiments, we evaluate DyBluRF model from two perspectives. First, we validate the quality of monocular video view synthesis from blurry videos using DyBluRF by comparing it to the SOTA novel view synthesis methods. Second, we demonstrate DyBluRF’s robustness in dynamic novel view synthesis against degrees of blurriness by comparing its performance with the existing dynamic novel view synthesis methods [19, 42], training them with either the original iPhone dataset [19] or our new Blurry iPhone dataset.

Dynamic Deblurring Novel View Synthesis. Tab. 1 shows the effectiveness of DyBluRF in dynamic deblurring novel view synthesis, comparing it to TiNeuVox [15], HexPlane [8], T-NeRF [19], HyperNeRF [42], 4D-GS [62], DP-NeRF [24], and BAD-NeRF [57], all optimized on our Blurry iPhone dataset. For the deblurring methods [24, 57] initially designed for static scenes, we add time embedding to their network inputs same as T-NeRF [19] in Tab. 1, resulting in BAD-NeRF_t and DP-NeRF_t, enabling dynamic component synthesis for a fair comparison. Additionally, we assess our DyBluRF against a cascade approach that combines GShiftNet [26], the SOTA 2D video deblurring method, with dynamic NeRFs (T-NeRF [19], HyperNeRF [42], and 4D-GS [62]). Note that for these cascades, we train them with the original camera poses from [19], bypassing our synthetic camera poses for a fair comparison. As detailed in Tab. 1, our DyBluRF significantly outperforms the existing SOTA methods across all metrics, especially demonstrating superior qualities in terms of perceptual quality (mLPIPS) and temporal consistency (tOF). Fig. 1 illustrates our method’s visual superiority. Further quantitative and qualitative analyses, along with a demo

video, are available in *Supplemental*. Using GShiftNet [26] as preprocessing for subsequent NeRF methods [19, 42, 62] improves perceptual quality (mLPIPS), but leads to more unstable structural qualities (mPSNR, mSSIM) and temporal consistency (tOF). These findings underscore that using 2D pixel-domain deblurring as preprocessing for subsequent dynamic NeRFs may be suboptimal. Finally, it is important to note that this cascade exhibits significantly poorer performance compared to DyBluRF, reinforcing DyBluRF’s advantages.

Robustness of DyBluRF against Degrees of Blurriness. Tab. 2 shows the robustness of DyBluRF across varying dataset capture qualities. We evaluate the dynamic novel view synthesis performance of T-NeRF [19], HyperNeRF [42], and DyBluRF by training each method with two datasets: the original iPhone dataset [19] or our newly synthesized Blurry iPhone dataset. As shown, both T-NeRF [19] and HyperNeRF [42] experience substantial performance declines across all metrics with the Blurry iPhone dataset compared to their performance with the original iPhone dataset [19], underscoring the challenge posed by our Blurry iPhone dataset for dynamic novel view synthesis without a deblurring module. In contrast, DyBluRF maintains consistent results between the two datasets across all metrics, demonstrating its robustness to different degrees of blurriness. We also visually analyze the robustness of DyBluRF against degrees of blurriness in Fig. 3. In Fig. 3-(a), we show the rendered color \hat{C}^{full} of the base ray (green boxes) and the averaged rendered color \hat{C}_B^{full} computed with Eq. (3) when trained with the Blurry iPhone dataset or the original iPhone dataset [19], respectively (blue boxes). As shown, DyBluRF adaptively predicts latent rays to stably model the physical blur process, maintaining the sharpness of the base ray’s rendering color \hat{C}^{full} regardless of the degrees of blurriness in the training frames. However, T-NeRF [19] and HyperNeRF [42] produce blurrier results with the Blurry iPhone dataset compared to the original iPhone dataset [19], as illustrated in Fig. 3-(b). Furthermore, as shown in Fig. 3-(c), the static deblurring NeRFs [24, 57] fail to learn the reliable sharp reconstruction from blurry training frames due to the absence of a temporal-aware deblurring module. We provide more details for latent sharp rays analyses in *Supplemental*.

Table 2: Robustness of DyBluRF against degrees of blurriness. ‘Trained w/ Original’ refers to training each model with the original iPhone dataset [19], while ‘Trained w/ Blurry’ applies to the Blurry iPhone dataset.

Method	Trained w/	mPSNR \uparrow	mSSIM \uparrow	mLPIPS \downarrow	tOF \downarrow
T-NeRF [19]	Original	16.96	0.577	0.379	0.843
	Blurry	16.15 -0.81	0.547 -0.030	0.456 +0.077	0.990 +0.147
HyperNeRF [42]	Original	16.81	0.569	0.332	0.869
	Blurry	15.30 -1.51	0.535 -0.034	0.447 +0.115	1.085 +0.216
DyBluRF (Ours)	Original	17.37	0.591	0.373	0.664
	Blurry	17.33 -0.04	0.591 -0.000	0.376 +0.003	0.675 +0.011

Table 3: Ablation study. ‘ \mathcal{L}_D ’ is [28]’s depth loss. ‘ \mathcal{N} ’ is the naive pose optimization [59], i.e., without interleave optimization. ‘2D’ is preprocessing with GShiftNet [26].

Variant	\mathcal{L}_{sm}	\mathcal{L}_{19}	BRI	MDD	mPSNR \uparrow	mSSIM \uparrow	mLPIPS \downarrow	tOF \downarrow
(a)	-	-	-	-	16.48	0.563	0.455	0.883
(b)	✓	-	-	-	16.85	0.572	0.422	0.714
(c)	✓	\mathcal{L}_D	-	-	15.13	0.528	0.666	1.063
(d)	✓	✓	-	-	17.18	0.590	0.426	0.692
(e)	✓	✓	-	2D	16.80	0.582	0.413	0.740
(f)	✓	✓	\mathcal{N}	-	16.06	0.545	0.449	0.806
(g)	✓	✓	-	✓	16.86	0.568	0.434	0.724
(h)	✓	✓	✓	-	17.24	0.593	0.413	0.653
(i)	✓	✓	✓	✓	17.33	0.591	0.376	0.675

4.2 Ablation Study

We conduct an ablation study to analyze the effectiveness of our \mathcal{L}_{sm} , \mathcal{L}_{lg} for dynamic scene reconstruction and our two-stage training strategy of BRI and MDD stages for deblurring dynamic radiance fields. Tab. 3 presents detailed quantitative results for the average performance across all scenes.

Unsupervised Staticness Maximization Loss (\mathcal{L}_{sm}). By incorporating \mathcal{L}_{sm} , DyBluRF effectively decomposes 3D scenes into static and dynamic components in an *unsupervised* manner. This aids our framework in more robustly reconstructing dynamic scenes, leading to performance gains as shown in variant (b) compared to variant (a). It is also worth noting that previous methods [18, 28, 31] only consider optical flows [52] for temporally close times to generate motion masks. This approach makes capturing long-range temporal cues challenging and results in inconsistent motion masks, as demonstrated in Fig. 4-(a). The use of these unstable masks leads to the misclassification of dynamic objects as static regions, undermining the multi-view consistency of the Static Net F_{θ^s} . In contrast, DyBluRF produces more consistent masks along the whole temporal axis, thanks to our \mathcal{L}_{sm} for unsupervised $M(\hat{r}_{p;t})$ training. Additionally, Fig. 4-(a) shows that the L1 loss of the logarithm helps overcome noisy motion prediction in $M(\hat{r}_{p;t})$, compared to the L2 loss of the logarithm (‘L2 of log’).

Local Geometry Variance Distillation (\mathcal{L}_{lg}). In Tab. 3, our \mathcal{L}_{lg} in variant (d) significantly improves the accuracy of 3D structures, surpassing variant (b), which does not incorporate geometry regularization. This enhancement is substantiated by higher mPSNR and mSSIM scores, and more consistent deformation across dynamic scenes, as denoted by the improved tOF. Additionally, variant (d) showcases the robustness of our \mathcal{L}_{lg} , outperforming the scale-invariant depth loss (‘ \mathcal{L}_D ’) [28] in variant (c). Fig. 4-(b) visualizes the effectiveness of our \mathcal{L}_{lg} by comparing it to the variants without geometry regularization (‘No reg.’) and with the scale-invariant depth loss [28]. Our \mathcal{L}_{lg} leads to better reconstruction of geometry for dynamic objects and novel view synthesis than the others.

BRI Stage. Our BRI in variant (h) outperforms variant (d) across all metrics. We analyze the critical role of our interleave optimization strategy in the BRI stage by omitting it in variant (f). As shown in Tab. 3, refining the base ray while optimizing radiance fields without the interleave optimization leads to adverse effects. As discussed in Sec. 3.1, F_{θ^d} can inadvertently compensate for base ray inaccuracies by learning unnecessary deformations. Hence, incorporating static geometry cues for precise base ray initialization is crucial, facilitated by our interleave optimization. Moreover, applying the MDD stage directly without a well-initialized base ray can deteriorate performance, as evidenced by the substantial performance gap between variants (i) and (g). This indicates that proper initialization of base rays by the BRI stage is crucial for subsequent deblurring.

MDD Stage. In Tab. 3, by comparing the final DyBluRF (i) with variant (h), we observe that the MDD stage significantly enhances the perceptual quality, as evidenced by the improved mLPIPS scores. Specifically, Fig. 4-(c) shows our DyBluRF’s effectiveness in novel view synthesis for video deblurring, attributed to the MDD stage’s adept handling of blurriness in textured regions. In addition,

as shown in Fig. 4-(d), our model more delicately decomposes the mixture of global camera and local object motions (i.e., white brick) across the training time indices. This results in robust novel view synthesis for a region where the object passes during training, compared to our variant not trained with LORR (Eq. (6)). Moreover, our final DyBluRF (i) significantly outperforms variant (e), the cascade of GShiftNet [26] and variant (d), emphasizing the advantages of full DyBluRF. Furthermore, variant (e) exhibits a slight improvement in mLPIPS but yields inferior mPSNR, mSSIM, and tOF compared to variant (d). This suggests that even though deblurring frames independently in the pixel domain reduces blurriness, it is hard to train precise spatio-temporal radiance fields.

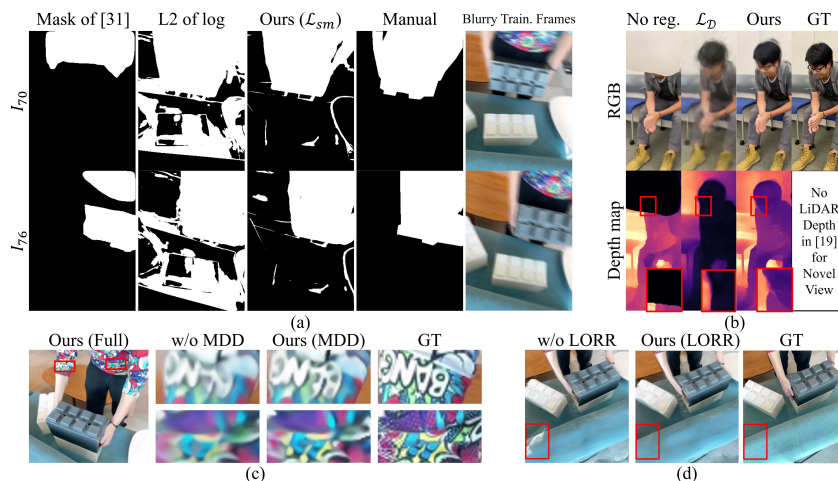


Fig. 4: Ablation study with visual comparisons. (a) ‘Mask of [31]’ indicates the preprocessed motion mask obtained using optical flows [52] from only consecutive frames and ‘L2 of log’ indicates the variant of our \mathcal{L}_{sm} to the L2 loss of the logarithm. ‘Manual’ indicates the manual annotation mask from RoboflowTM [1]. ‘Blurry Train. Frames’ indicates the corresponding blurry train frame of our Blurry iPhone dataset. Please note that our motion mask is all white when trained without \mathcal{L}_{sm} . (b) ‘No reg.’ indicates the variant without any loss for geometry. ‘Ours’ refers to our \mathcal{L}_{lg} . Ablation Studies on (c) the MDD stage (Sec. 3.4) and (d) the LORR (Eq. (6)).

5 Conclusion

We *first* propose a novel dynamic deblurring NeRF for blurry monocular video, called DyBluRF, which can effectively render the sharp novel spatio-temporal views from blurry monocular frames with inaccurate camera poses. DyBluRF consists of a two-stage framework, including the BRI stage and the MDD stage. The BRI stage simultaneously reconstructs dynamic 3D scenes and initializes better base rays. The MDD stage introduces a novel ILSP approach to decompose latent sharp rays into global camera and local object motion components. We also incorporate simple yet effective \mathcal{L}_{sm} and \mathcal{L}_{lg} for stable training dynamic radiance field. Experimental results demonstrate that DyBluRF outperforms recent SOTA methods both qualitatively and quantitatively.

DyBluRF: Dynamic Deblurring Neural Radiance Fields for Blurry Monocular Video

- Supplementary Material -

Minh-Quan Viet Bui^{1*}, Jongmin Park^{1*}, Jihyong Oh^{2†}, and Munchurl Kim^{1†}

¹ KAIST, ² Chung-Ang University
 {bvmquan, jm.park, mkimee}@kaist.ac.kr jihyongoh@cau.ac.kr
<https://kaist-viclab.github.io/dyblurf-site/>

A Detailed Process of DyBluRF Framework

We detail the optimization process of our DyBluRF framework with two pseudocodes mentioned in the main paper: the BRI stage in Algorithm 1 and the overall process in Algorithm 2. Additionally, we describe the inference process of our DyBluRF in Algorithm 3. It should be noted that our whole two-stage framework including losses in the training phase, enhances our Static Net F_{θ^s} and Dynamic Net F_{θ^d} , allowing them to synthesize a sharper rendered color from each single input ray $\mathbf{r}_{\mathbf{p};t}^{inf}$ for Algorithm 3.

Algorithm 1 Base Ray Initialization (BRI) Stage

```

1: procedure BRI( $F_{\theta^s}, F_{\theta^d}, \mathcal{S}_t$ )
2:   for it = 0 to  $2 \times 10^5$  do
3:     Sample random rays  $\tilde{\mathbf{r}}_{\mathbf{p};t}$ 
4:     Compute base ray  $\hat{\mathbf{r}}_{\mathbf{p};t} \leftarrow \mathcal{W}(\tilde{\mathbf{r}}_{\mathbf{p};t}, \mathcal{S}_t)$  (Eq. (4))
5:     if it|2 then                                     ▷ Static Net and Ray Warp.
6:       Compute  $\hat{\mathbf{C}}^s(\hat{\mathbf{r}}_{\mathbf{p};t}), \mathbf{M}(\hat{\mathbf{r}}_{\mathbf{p};t})$ 
7:        $loss \leftarrow \mathcal{L}_{photo}(\hat{\mathbf{C}}^s(\hat{\mathbf{r}}_{\mathbf{p};t}))$  (Eq. (8))
8:       Update Static Net  $F_{\theta^s}, \mathcal{S}_t$ 
9:     else                                             ▷ Dynamic Net and Static Net
10:      Compute  $\hat{\mathbf{C}}^s(\hat{\mathbf{r}}_{\mathbf{p};t}), \hat{\mathbf{C}}^d(\hat{\mathbf{r}}_{\mathbf{p};t}), \mathbf{M}(\hat{\mathbf{r}}_{\mathbf{p};t})$ 
11:      Compute  $\hat{\mathbf{C}}^{full}(\hat{\mathbf{r}}_{\mathbf{p};t})$  (Eq. (1))
12:       $loss \leftarrow \mathcal{L}_{photo}(\hat{\mathbf{C}}^s(\hat{\mathbf{r}}_{\mathbf{p};t})) + \mathcal{L}_{photo}(\hat{\mathbf{C}}^{d,full}(\hat{\mathbf{r}}_{\mathbf{p};t})) + \mathcal{L}_{sm} + \mathcal{L}_{lg}$ 
           (Eq. (7), Eq. (8), Eq. (10))
13:      Update Static Net  $F_{\theta^s}$ , Dynamic Net  $F_{\theta^d}$ 
14:    end if
15:  end for
16: end procedure

```

* Co-first authors (equal contribution), † Co-corresponding authors

Algorithm 2 Overall Training Process of DyBluRF

```

1: Init  $F_{\theta^s}, F_{\theta^d}, F_{\theta^l}, \mathcal{S}_t, \mathcal{S}_{t;q}^g$ 
2: Do BRI( $F_{\theta^s}, F_{\theta^d}, \mathcal{S}_t$ ) (Fig. 2-(a) and Algorithm 1)
3: for it = 0 to  $10^5$  do ▷ MDD (Sec. 3.4 and Fig. 2-(b))
4:   Sample random rays  $\tilde{\mathbf{r}}_{\mathbf{p};t}$ 
5:   Compute base ray  $\hat{\mathbf{r}}_{\mathbf{p};t} \leftarrow \mathcal{W}(\tilde{\mathbf{r}}_{\mathbf{p};t}, \mathcal{S}_t)$  (Eq. (4)) ▷ Freeze  $\mathcal{S}_t$ 
6:   Compute  $\hat{\mathbf{C}}^{s,d,full}(\hat{\mathbf{r}}_{\mathbf{p};t}), \mathbf{M}(\hat{\mathbf{r}}_{\mathbf{p};t})$ 
7:    $\{\hat{\mathbf{r}}_{\mathbf{p};t;q}^g\}_{q=1}^{N_b} \leftarrow \{\mathcal{W}(\hat{\mathbf{r}}_{\mathbf{p};t}, \mathcal{S}_{t;q}^g)\}_{q=1}^{N_b}$  (Eq. (5)) ▷ GCRP
8:   if  $\mathbf{M}(\hat{\mathbf{r}}_{\mathbf{p};t}) = 0$  then ▷ Only global camera motion
9:     for  $q = 1$  to  $N_b$  do
10:        $\dot{\mathbf{r}}_{\mathbf{p};t;q} \leftarrow \hat{\mathbf{r}}_{\mathbf{p};t;q}^g$ 
11:       Compute  $\hat{\mathbf{C}}^{s,d,full}(\dot{\mathbf{r}}_{\mathbf{p};t;q})$ 
12:     end for
13:   else if  $\mathbf{M}(\hat{\mathbf{r}}_{\mathbf{p};t}) = 1$  then ▷ Both global camera and local object motions
14:     for  $q = 1$  to  $N_b$  do
15:        $\mathcal{S}_{\mathbf{p};t;q}^l \leftarrow F_{\theta^l}(\lceil \phi(\hat{\mathbf{r}}_{\mathbf{p};t;q}^g), l(t) \rceil)$ 
16:        $\dot{\mathbf{r}}_{\mathbf{p};t;q}^l \leftarrow \mathcal{W}(\hat{\mathbf{r}}_{\mathbf{p};t;q}^g, \mathcal{S}_{\mathbf{p};t;q}^l)$  (Eq. (6)) ▷ LORR
17:        $\dot{\mathbf{r}}_{\mathbf{p};t;q} \leftarrow \dot{\mathbf{r}}_{\mathbf{p};t;q}^l$ 
18:       Compute  $\hat{\mathbf{C}}^{s,d,full}(\dot{\mathbf{r}}_{\mathbf{p};t;q})$ 
19:     end for
20:   end if
21:    $\hat{\mathbf{C}}_{\mathbf{B}}^{s,d,full}(\hat{\mathbf{r}}_{\mathbf{p};t}) \leftarrow \mathcal{A}(\hat{\mathbf{C}}^{s,d,full}(\hat{\mathbf{r}}_{\mathbf{p};t}), \{\hat{\mathbf{C}}^{s,d,full}(\dot{\mathbf{r}}_{\mathbf{p};t;q})\}_{q=1}^{N_b})$  (Eq. (3))
22:    $loss \leftarrow \mathcal{L}_{mphoto}(\hat{\mathbf{C}}_{\mathbf{B}}^s(\hat{\mathbf{r}}_{\mathbf{p};t})) + \mathcal{L}_{photo}(\hat{\mathbf{C}}_{\mathbf{B}}^{d,full}(\hat{\mathbf{r}}_{\mathbf{p};t})) + \mathcal{L}_{sm} + \mathcal{L}_{lg}$ 
23:   Update Static Net  $F_{\theta^s}$ , Dynamic Net  $F_{\theta^d}, F_{\theta^l}, \mathcal{S}_{t;q}^g$ 
24: end for

```

Algorithm 3 Inference Process

```

1: procedure INFERENCE( $F_{\theta^s}, F_{\theta^d}, \mathbf{r}_{\mathbf{p};t}^{inf}$ )
2:   for n = 0 to 128 do
3:     Sampling point  $\mathbf{x}_n$  on inference target ray  $\mathbf{r}_{\mathbf{p};t}^{inf}$ 
4:      $\mathbf{c}_n^s, \sigma_n^s, p(st|\mathbf{x}_n) \leftarrow F_{\theta^s}(\gamma(\mathbf{x}_n), \mathbf{d})$ 
5:      $\mathbf{c}_n^d, \sigma_n^d \leftarrow F_{\theta^d}(\gamma(\mathbf{x}_n), \mathbf{d}), l(t)$ 
6:   end for
7:   Compute  $\hat{\mathbf{C}}^{full}(\mathbf{r}_{\mathbf{p};t}^{inf})$  (Eq. (1))
8: end procedure

```

B Detailed Process of Synthesis Blurry iPhone dataset

We provide the detailed process of synthesizing our proposed Blurry iPhone dataset which includes blurry RGB frames and the corresponding camera poses. To synthesize a blurry video frame \mathcal{B}_t , we apply the VFI method [50] to the original iPhone dataset [19]. This method generates seven interpolated frames between each pair of consecutive original video frames (\mathcal{I}_{t-1} and \mathcal{I}_t , \mathcal{I}_t and \mathcal{I}_{t+1}). We then select seven specific frames, ranging from $\mathcal{I}_{t-\frac{5}{8}}$ to $\mathcal{I}_{t+\frac{3}{8}}$, and average them to create the final blurry frame \mathcal{B}_t . Fig. 5 illustrates the visualization of synthesized blurry frames by comparing them to the direct averaging of three original consecutive frames \mathcal{I}_{t-1} , \mathcal{I}_t , and \mathcal{I}_{t+1} , without applying the VFI method [50]. As shown, the synthesis process of our DyBluRF results in much natural and realistic blurriness than the direct averaging.

Accompanying each blurry frame in the training dataset, we also synthesize the corresponding inaccurate camera pose $\tilde{\mathcal{P}}_t = [\tilde{\mathcal{R}}_t | \tilde{\mathcal{T}}_t]$ by simulating a smooth camera trajectory in 3D space [2, 23]. More specifically, in [2], the authors utilize a quaternion spherical linear interpolation (Slerp) approach to synthesize intermediate camera poses between two specific camera poses. This process generates the corresponding intermediate images required for the blur modeling process. Following this methodology, in the synthesis of the rotation matrix $\tilde{\mathcal{R}}_t$, we generate interpolated rotation matrices between each pair of original rotation matrices using Slerp. We then select the seven rotation matrices, ranging from $\mathcal{R}_{t-\frac{5}{8}}$ to $\mathcal{R}_{t+\frac{3}{8}}$, and compute their average to be used for the corresponding blurry frame \mathcal{B}_t . Since directly calculating the average of multiple rotation matrices is challenging, we convert these matrices into quaternions before averaging them. The resultant $\tilde{\mathcal{R}}_t$ appropriately simulates the 3D camera motion during the blur modeling process [2, 23]. Similar to the process with the rotation matrix $\tilde{\mathcal{R}}_t$, for the synthesis of the translation matrix $\tilde{\mathcal{T}}_t$, we adopt linear interpolation to generate interpolated matrices. We then average the seven matrices, ranging from $\mathcal{T}_{t-\frac{5}{8}}$ to $\mathcal{T}_{t+\frac{3}{8}}$. The resulting interpolated camera pose $\tilde{\mathcal{P}}_t$ has different rotation and translation matrices with the original camera pose \mathcal{P}_t , making it more challenging for existing methods [8, 15, 24, 33, 42, 57] to reconstruct the correct geometry of a scene, except for our DyBluRF.

C Implementation Details

Our DyBluRF is implemented using JAX and built upon Dycheck [19] codebase. Similar to Dycheck [19], we adopt $N = 128$ samples for casted each ray. Our model undergoes training for 2×10^5 iterations in the BRI stage and 1×10^5 in the MDD stage. The hyperparameters for the loss weighting coefficients, denoted as λ_{lg} and λ_{sm} , are empirically set to 0.075 and 0.002, respectively. For all scenes, our best model is configured with a fixed number of latent sharp rays $N_b = 6$. We utilize the Adam optimizer with exponential scheduling for training our networks. Notably, the learning rates for the screw axis embeddings \mathcal{S}_t and $\mathcal{S}_{t,q}^g$ are in the range $[10^{-4}, 10^{-6}]$, while the learning rates for the remaining

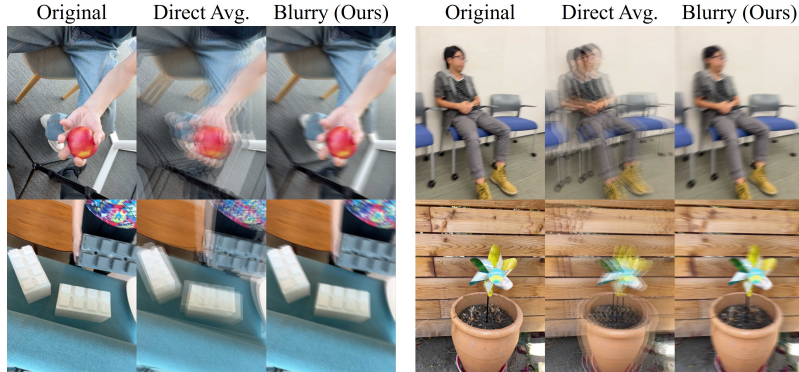


Fig. 5: Visualizations of the blurry frame synthesis. Our synthesized blurry frames, using the VFI method [50], exhibit more realistic and natural blurriness compared to the direct averaging of three consecutive original frames (‘Direct Avg.’).

MLPs are in the range $[10^{-3}, 10^{-4}]$. For the implementation of the Static Net F_{θ_s} and Dynamic Net F_{θ_d} of the main paper, we adopt the NeRF architecture from the Dycheck [19] codebase to ensure a fair comparison. This NeRF architecture comprises a trunk MLP, a sigma MLP and an rgb MLP. The sigma and rgb MLPs take the output feature of the trunk MLP as their respective inputs. We configure the number of layers for the trunk, sigma, and rgb MLPs to be 9, 1, and 2, respectively. The dimensions of the hidden layer for the trunk and rgb MLPs are set to 256 and 128, respectively. For the Static Net, we introduce a blending MLP that consists of a single layer. This MLP takes the output of the trunk MLP as input to produce the staticness probability $p(\text{st}|\mathbf{x})$. For the local object-motion MLP F_{θ_l} , we set the number of layers and dimension of hidden layers to 8 and 128, respectively. We set the number of frequencies for each positional encoding γ of 3D sample positions \mathbf{x} and their corresponding viewing directions \mathbf{d} to 8 and 4, respectively. We also set the output dimension of the time encoding $l(t)$ to 8 and the number of samples for the discretized ray embedding ϕ to 32. We recommend readers to refer to our project page at <https://kaist-viclab.github.io/dyblurf-site/>, which provides source codes and pretrained models for the sake of *reproducibility*.

D Additional Experimental Results

D.1 Robustness of DyBluRF against Degrees of Blurriness

We further visualize the extended version of Fig. 3-(a) from the main paper in Fig. 6 to demonstrate our DyBluRF’s optimization capacity for adapting to varying degrees of blurriness. Fig. 6 displays the full rendered colors $\{\hat{\mathbf{C}}^{full}(\hat{\mathbf{r}}_{\mathbf{p};t;q})\}_{q=1}^{N_b}$ of all $N_b (= 6)$ latent sharp rays, $\hat{\mathbf{C}}^{full}(\hat{\mathbf{r}}_{\mathbf{p};t})$ of the base ray, and the averaged rendered color $\hat{\mathbf{C}}_{\mathcal{B}}^{full}(\hat{\mathbf{r}}_{\mathbf{p};t})$ computed with Eq. (3), produced by

our DyBluRF when trained respectively with the Blurry iPhone dataset or the original iPhone dataset [19]. As illustrated in Fig. 6-(a), our DyBluRF adaptively predicts diverse latent sharp rays based on the base ray to effectively render the averaged blurry color corresponding to the physical blur process (‘GT (Train)’) when trained with the Blurry iPhone dataset. On the other hand, in Fig. 6-(b), the rendered colors exhibit remarkable consistency across all latent sharp rays as well as the base ray. This consistency results in a relatively sharp averaged color that closely aligns with the training frames found in the original iPhone dataset [19]. We also compare the average standard deviations of the color (σ_C^{avg}), ray origin (σ_o^{avg}), and ray direction (σ_d^{avg}), respectively, for all latent sharp rays and the base ray, as trained with each dataset. As demonstrated, the standard deviation of all values is significantly larger when trained with the Blurry iPhone dataset compared to the original iPhone dataset [19]. This underscores the robustness of our DyBluRF’s optimization capacity in handling varying degrees of blurriness.

D.2 Comparison with the SOTA Methods with Original iPhone Dataset

In Tab. 4, we present the performance metrics of dynamic novel view synthesis as produced by various models: NSFF [28], T-NeRF [19], HyperNeRF [42], RoDynRF [31], and 4D-GS [62], all of which are trained using the original iPhone dataset [19]. Moreover, we compare these results against those of our DyBluRF, evaluating its performance when trained on both the original iPhone dataset [19] or our Blurry iPhone dataset. As illustrated in Tab. 4, DyBluRF, when trained with the original iPhone dataset [19], outperforms all compared methods significantly in terms of mPSNR, mSSIM, and tOF. Please note that even though mLPIPS of HyperNeRF [42] is better than two types of ours, it does not result in smoother video rendering in terms of much larger tOF (temporal consistency), which is an important visual factor for video view synthesis. Furthermore, we observe that HyperNeRF [42] exhibits inconsistent artifacts in dynamic regions, as illustrated in Fig. 7. These superior performances are attributed to DyBluRF’s innovatively designed framework, incorporating our novel Unsupervised Staticness Maximization loss (\mathcal{L}_{sm}) and Local Geometry Variance Distillation (\mathcal{L}_{lg}). These components are specifically tailored to optimize radiance fields effectively from highly dynamic monocular videos. Moreover, DyBluRF exhibits consistent dynamic novel view synthesis performances when trained on the Blurry iPhone dataset, thanks to our advanced motion-aware deblurring method, which comprises the BRI stage and the MDD stage. For NSFF [28], since Dycheck [19] does not provide an implementation of NSFF [28], we attempted to reproduce it. However, our version did not achieve results comparable to the benchmark in Dycheck [19]. Therefore, we directly bring the results of NSFF provided in Dycheck [19] for optimal performances, which do not include tOF.

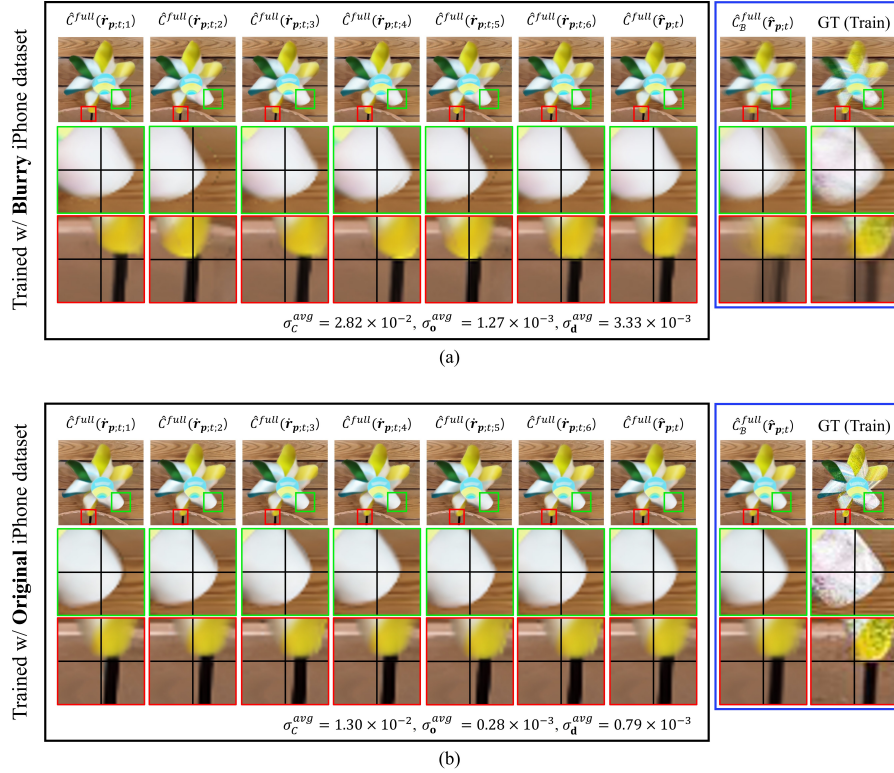
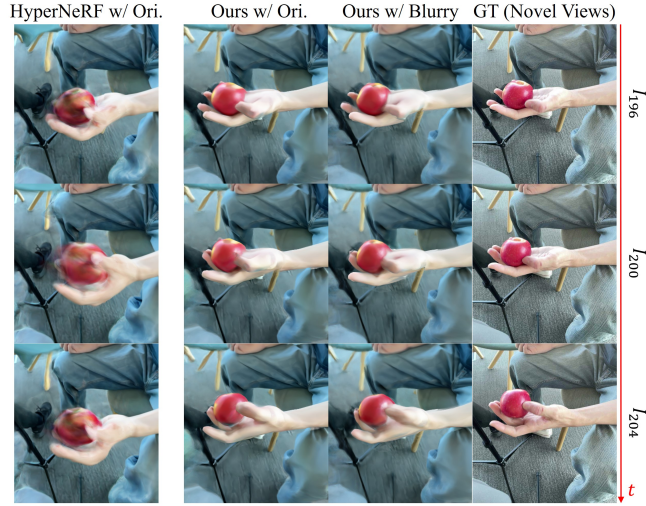
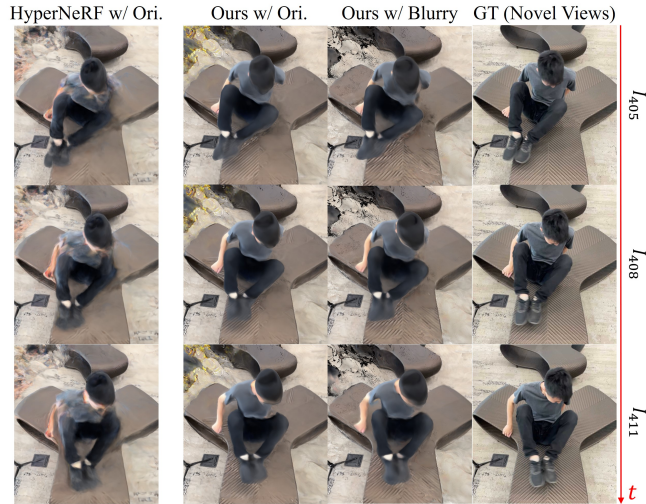


Fig. 6: Robustness of DyBluRF against degrees of blurriness. We visualize the rendering frames which refer to each rendered color $\hat{\mathbf{C}}^{full}(\hat{\mathbf{r}}_{\mathbf{p};t;q}$ of q^{th} latent sharp ray, $\hat{\mathbf{C}}^{full}(\hat{\mathbf{r}}_{\mathbf{p};t})$ of the base ray, and the averaged rendered color $\hat{\mathbf{C}}_B^{full}(\hat{\mathbf{r}}_{\mathbf{p};t})$ computed with Eq. (3). These are produced by our DyBluRF when trained with (a) the Blurry iPhone dataset and (b) the original iPhone datasets [19], respectively. ‘ σ_C^{avg} ’, ‘ σ_o^{avg} ’, and ‘ σ_d^{avg} ’ refer to the average standard deviations of the color, ray origin, and ray direction, respectively, for all latent sharp rays and the base ray.



(a)



(b)

Fig. 7: Visual comparisons between our DyBluRF and HyperNeRF [42] for (a) *Apple* scene and (b) *Spin* scene. We compare our DyBluRF, trained on either the Blurry (‘Ours w/ Blurry’) or the original (‘Ours w/ Ori.’) iPhone datasets, with HyperNeRF [42] trained on the original iPhone dataset [19] (‘HyperNeRF w/ Ori.’). Notably, HyperNeRF frequently produces inconsistent artifacts in dynamic regions.

Table 4: Dynamic novel view synthesis evaluation. ‘Trained w/ Original’ refers to training each model with the original iPhone dataset [19], while ‘Trained w/ Blurry’ applies to the Blurry iPhone dataset. **Red** and **blue** denote the best and second best performances, respectively.

Method	Trained w/	mPSNR \uparrow	mSSIM \uparrow	mLPIPS \downarrow	tOF \downarrow
NSFF [28]	Original	15.46	0.569	0.396	-
T-NeRF [33]	Original	16.96	0.577	0.379	0.843
HyperNeRF [42]	Original	16.81	0.550	0.332	0.869
RoDynRF [31]	Original	17.09	0.534	0.517	0.979
4D-GS [62]	Original	13.16	0.448	0.527	1.110
DyBluRF (Ours)	Original	17.37	0.591	0.373	0.664
DyBluRF (Ours)	Blurry	17.33	0.591	0.376	0.675

Table 5: Additional comparisons with BAD-NeRF [57]. We try different reproduction strategies to decide the appropriate comparison with prior static deblurring NeRFs [24, 57].

Method	mPSNR \uparrow	mSSIM \uparrow	mLPIPS \downarrow	tOF \downarrow
BAD-NeRF [57]	10.01	0.416	0.749	0.755
BAD-NeRF $_t$ [57]	10.93	0.446	0.705	1.464
BAD-NeRF $_t$ [57] + \mathcal{L}_{sm} + \mathcal{L}_{lg}	11.80	0.468	0.630	1.500
DyBluRF (Ours)	17.33	0.591	0.376	0.675

D.3 Enhancing BAD-NeRF with Our Framework

In Tab. 5, we present benchmark numbers for the original BAD-NeRF [57] code trained on our Blurry iPhone dataset. Notably, the static variant of BAD-NeRF [57] faces challenges in accommodating dynamic object deformations, resulting in lower mPSNR and mSSIM values. This limitation arises from its inherent design, which is designed only for static scenes, resulting in higher tOF which actually means degenerated static rendering. Furthermore, we have investigated improvements to the BAD-NeRF [57] approach by integrating our novel \mathcal{L}_{sm} and \mathcal{L}_{lg} losses. Specifically, we exclude our motion-aware deblurring strategies, including the BRI and MDD stages, from the final DyBluRF model. Subsequently, we employ our decomposed radiance fields, F_{θ^s} and F_{θ^d} , along with our proposed optimization losses, finely tuned hyperparameters, and reimplement BAD-NeRF [57]’s deblurring strategy within our codebase, denoted as ‘BAD-NeRF $_t$ [57] + \mathcal{L}_{sm} + \mathcal{L}_{lg} ’ in Tab. 5. This improved version shows enhanced performance compared to other static deblurring NeRF implementations. However, without our specialized motion-aware deblurring strategies, especially the BRI and MDD stages, the radiance fields struggle to achieve high-quality reconstructions of monocular blurry videos. We conducted similar experiments for DP-NeRF [24], which show that the static version of DP-NeRF [24] obtains met-

rics of 10.62/0.411/0.705/0.717. In the case of ‘DP-NeRF_t [24] + $\mathcal{L}_{sm} + \mathcal{L}_{lg}$ ’, the complexity of its codebase presented significant challenges, preventing us from crafting an effective enhancement for DP-NeRF [24].

D.4 Overfitting Issues of the Existing Methods

Fig. 8 shows the rendered frames from HexPlane [8], DP-NeRF_t [24], and BAD-NeRF_t [57] using the training camera pose, a nearby test camera pose, and a distant test camera pose, all at the specific time index t_{200} , respectively. As demonstrated, the quality of the rendered frame using a test camera pose distant from the training cameras is substantially poorer than the rendering qualities from training camera pose and nearby camera pose. These overfitting issues may be caused by the highly monocular characteristic of the Blurry iPhone dataset. Specifically, for HexPlane [8], the author indicates in the third and sixth replies on HexPlane’s GitHub issue #7 that the architecture also performs poorly on the original iPhone dataset [19], potentially due to the dataset’s monocular setting (<https://github.com/Caoang327/HexPlane/issues/7>).

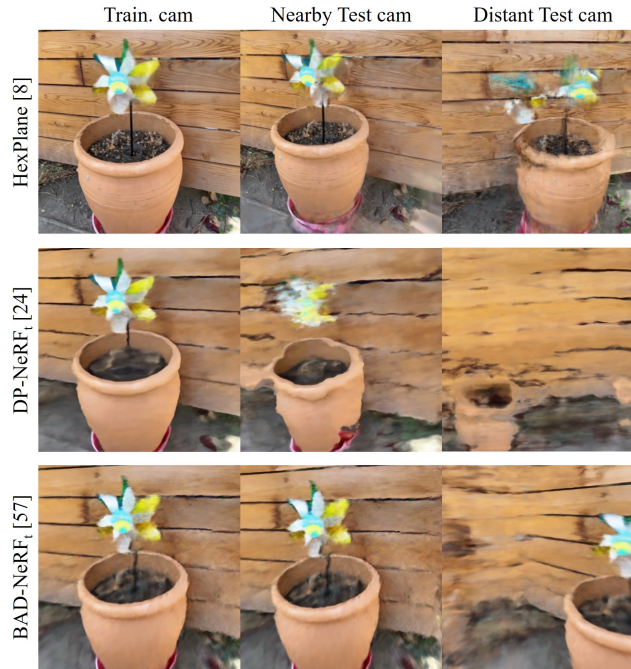


Fig. 8: The rendered frames by HexPlane [8], DP-NeRF_t [24], and BAD-NeRF_t [57] using the training camera pose (‘Train. cam’), a nearby test camera pose (‘Nearby Test cam’), and a distant test camera pose (‘Distant Test cam’), all at t_{200} , respectively.

D.5 Additional Qualitative Comparisons

Fig. 13 and Fig. 14 show the additional visual comparisons for dynamic deblurring novel view synthesis. Our DyBluRF generally synthesizes *temporally consistent* deblurring results better, results that are often not achieved by previous methods [8, 42, 57].

D.6 Visual Comparisons with Demo Video

We provide a video at <https://www.youtube.com/watch?v=jJeUCPW1sDA&t=2s> for comparing our DyBluRF with the existing methods: BAD-NeRF [57], DP-NeRF [24], HexPlane [8], 4D-GS [62], the cascade of GShiftNet [26] and T-NeRF [19], T-NeRF [19], and HyperNeRF [42] for (A) Varying Time & Fixed Pose on *Spin* scene, (B) Varying Pose & Fixed Time on *Apple* scene, and (C) Varying Both Pose & Time on *Block* scene. Moreover, we show the predicted motion masks by our DyBluRF in an *unsupervised* manner and compare it with the pre-computed motion masks from RoDynRF [31] on *Wheel* scene.

D.7 Complexity Comparison

We compare the inference time and the number of parameters of our DyBluRF to the existing methods by using a single RTX 3090 Ti in Tab. 6. Please note that our framework primarily focuses on improving the handling of novel problems associated with dynamic deblurring in NeRF. To make our work faster and lighter, we plan to enhance it by integrating dynamic methods based on Gaussian Splatting, such as 4D-GS [62].

Table 6: Complexity comparison. We measure the performances on a single RTX 3090 Ti for the image resolution of 480×360 .

Method	Inference Time (sec/frame)	# of Parameters (M)
TiNeuVox [15]	1.5	24.83
HexPlane [8]	2.2	9.73
T-NeRF [19]	5.0	1.19
HyperNeRF [42]	7.5	1.31
4D-GS [62]	0.05	39.29
DP-NeRF _t [24]	4.3	1.34
BAD-NeRF _t [57]	4.4	1.22
DyBluRF (Ours)	9.1	1.78

E Additional Ablation Study

E.1 Binary Motion Mask Prediction

As discussed in Sec. 3.2 of the main paper, we utilize the Static Net F_{θ_s} to predict the staticness probability $p(\text{st}|\mathbf{x}_n)$ for each n^{th} 3D sampling point \mathbf{x}_n along the ray $\hat{\mathbf{r}}_{\mathbf{p};t}$ in order to predict the binary motion mask $\mathbf{M}(\hat{\mathbf{r}}_{\mathbf{p};t})$ for the decomposition of static and dynamic scene components. Since the staticness probability $p(\text{st}|\mathbf{x}_n)$ for a 3D point \mathbf{x}_n in the scene remains consistent regardless of the cast ray and the time index, it can be accurately predicted using only the Static Net F_{θ_s} without requiring any time instance as input. To demonstrate the effectiveness of our strategy for binary motion mask prediction, we compare our predicted binary motion mask $\mathbf{M}(\hat{\mathbf{r}}_{\mathbf{p};t})$ produced by the Static Net with a variant that uses the Dynamic Net F_{θ_d} (with additional time t embedding) instead of the Static Net to predict $p(\text{st}|\mathbf{x}_n, \hat{\mathbf{r}}_{\mathbf{p};t})$, in Fig. 9. As demonstrated, the predicted binary motion mask using the Dynamic Net F_{θ_d} is substantially noisier, indicating that static regions are misclassified as dynamic regions. This result is attributed to the variant that treats the dynamicness probability as a *time-variant* factor as in [18, 31], potentially leading to overparameterization. On the other hand, treating this probability as *time-invariant* simplifies the model and effectively eliminates motion misclassification noise in the final *un-supervised* binary motion mask, $\mathbf{M}(\hat{\mathbf{r}}_{\mathbf{p};t})$, thereby ensuring more stable motion segmentation.



Fig. 9: Binary motion mask prediction. ‘ M by Dynamic Net’ indicates the predicted binary motion mask using the Dynamic Net, similar to [18, 31], and ‘ M by Static Net (Ours)’ indicates the predicted binary motion mask using the Static Net.

E.2 Local Geometry Variance Distillation (\mathcal{L}_{lg}).

Let $\mathcal{D}_{\mathbf{p};t}^*$ represent the absolute scale depth values obtained from the LiDAR sensor. The scale-ambiguity depth $\mathcal{D}_{\mathbf{p};t}$ defined in Sec. 3.5 can be expressed as a linear transformation of $\mathcal{D}_{\mathbf{p};t}^*$ using the scalars a, b as:

$$\mathcal{D}_{\mathbf{p};t} = a\mathcal{D}_{\mathbf{p};t}^* + b. \quad (11)$$

As elaborated in Sec. 3.5, our loss function \mathcal{L}_{lg} effectively addresses both scale and shift ambiguities as follows:

$$\begin{aligned} \mathbf{g}_{\mathbf{p};t} &= \overline{\left(\frac{\partial \hat{\mathbf{r}}_{\mathbf{p};t}(a\mathcal{D}_{\mathbf{p};t}^* + b)}{\partial p_u} \times \frac{\partial \hat{\mathbf{r}}_{\mathbf{p};t}(a\mathcal{D}_{\mathbf{p};t}^* + b)}{\partial p_v} \right)} \\ &= \overline{\left(\frac{\partial \hat{\mathbf{r}}_{\mathbf{p};t}(a\mathcal{D}_{\mathbf{p};t}^*)}{\partial p_u} \times \frac{\partial \hat{\mathbf{r}}_{\mathbf{p};t}(a\mathcal{D}_{\mathbf{p};t}^*)}{\partial p_v} \right)} \\ &= \mathbf{g}_{\mathbf{p};t}^*, \end{aligned} \quad (12)$$

where $\mathbf{g}_{\mathbf{p};t}^*$ represents the local geometry variance computed from the absolute scale depths. To further demonstrate the robustness of \mathcal{L}_{lg} , we train DyBluRF on the ‘Block’ scene from the Blurry iPhone dataset, utilizing LiDAR depth values provided in [19]. The result of this experiment is 17.39/0.664/0.361/0.735, which exhibits a marginal improvement over ‘Ours’ as detailed in Tab. 1. Consequently, our \mathcal{L}_{lg} regularization shows robustness across different types of depth data. It should be noted that as LiDAR is often absent in benchmark datasets and casually-captured videos from general users, our \mathcal{L}_{lg} can be adopted to effectively resolve monocular depth ambiguity.

E.3 Base Ray Initialization (BRI) Stage.

To demonstrate the superiority of our proposed interleave optimization strategy in our BRI stage, we measure the discrepancy between the initialized base ray with the corresponding ray from the original iPhone dataset [19] and compare it to the variant without the interleave optimization, in Tab. 7 and Fig. 10. As illustrated in Tab. 7 and Fig. 10 and discussed in Sec. 3.3, optimizing the dynamic radiance field and initializing the base rays at the same training iteration may lead to suboptimal local minima. In contrast, our DyBluRF, by adopting interleave optimization alongside the static geometry cues, achieves a more stable base ray initialization from the input training ray $\tilde{\mathbf{r}}_{\mathbf{p};t}$.

E.4 Local Object-motion-aware Ray Refinement (LORR).

We provide additional visualizations to illustrate the varying rendering quality of the model without local object motion learning and the final DyBluRF in Fig. 11. Our final model excels at finely breaking down the blend of global camera motion and local object motions throughout the training times. This leads to a strong and reliable synthesis of novel views for our final DyBluRF, in contrast to our variant that wasn’t trained with LORR (Eq. (6)).

Table 7: Average discrepancy between the initialized base ray with the corresponding ray from the original iPhone dataset [19]. We compare the average discrepancy of origin (Dis_o) and direction (Dis_d) of our DyBluRF with the variant without interleave optimization in the BRI stage.

Variant	$\text{Dis}_o \downarrow$	$\text{Dis}_d \text{ (}^\circ\text{)} \downarrow$
w/o interleave optimization	0.00899	0.00914
Ours (w/ interleave optimization)	0.00697	0.00871

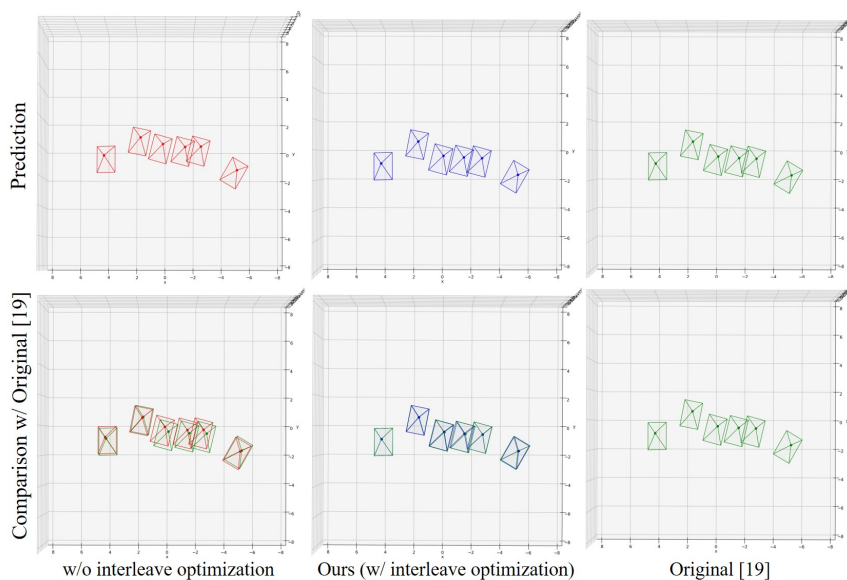


Fig. 10: Visualization of discrepancy between the initialized base rays and the corresponding rays from the original iPhone dataset [19]. To qualitatively compare the initialized base rays, we visualize their corresponding camera frustums. Note that each camera frustum represents a set of base rays cast from the same camera instance. In the first row, we show the camera frustums predicted by the variant without interleave optimization (Red), our DyBluRF with interleave optimization (Blue), and the corresponding camera frustums from the original iPhone dataset [19] (Green). In the second row, we directly overlap each predicted camera frustum with the corresponding original camera frustum from Dycheck [19].

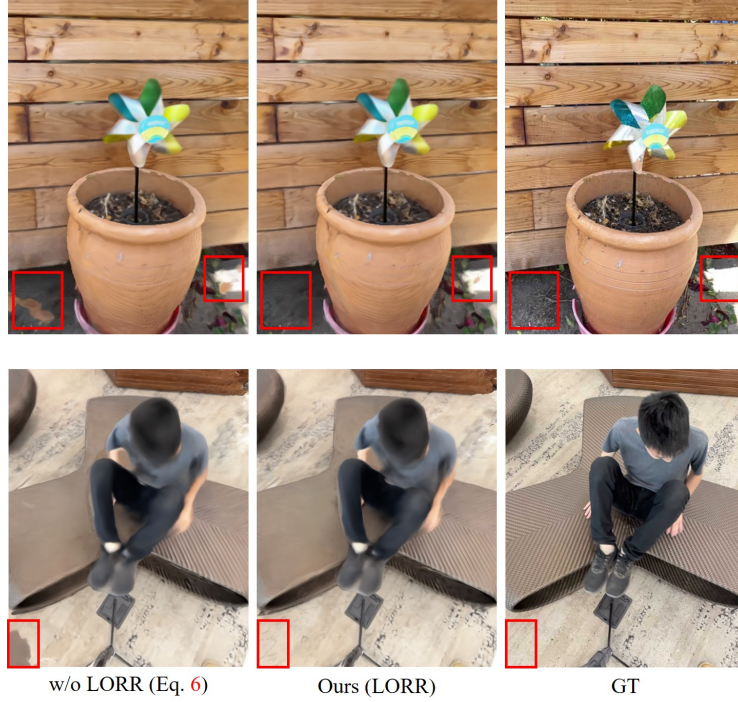


Fig. 11: Visualization of rendering quality improvement using motion decomposition.

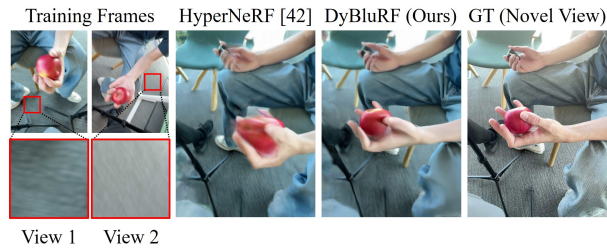


Fig. 12: Limitations of our DyBluRF. Since the majority of training video frames in the Blurry iPhone dataset exhibit a similar tone in View 1 (about 92% of the training frames), reconstructing the accurate tone of validation views with a similar tone in View 2 (about 8% of the training frames) becomes challenging. This difficulty arises due to the varying lighting effects present in the Blurry iPhone dataset.

E.5 The Number of Latent Sharp Rays

We provide a quantitative comparison of our DyBluRF model with varying numbers of latent sharp rays for the MDD stage in Tab. 8. In particular, increasing the number N_b of latent sharp rays can improve the reconstruction performance but it requires more computational cost. For the best quality and computational efficiency, we adopt $N_b = 6$ for all experiments of the final DyBluRF. To measure the training time per iteration, we utilize a single RTX 3090Ti GPU and set the batch size to 128. It is notable that the number of N_b only affects the training time. In the inference stage, where we render a single predicted sharp ray per pixel, the inference time remains constant across all variants, irrespective of the different values of N_b .

Table 8: Ablation Study on the number of latent sharp rays.

N_b	mPSNR \uparrow	mSSIM \uparrow	mLPIPS \downarrow	tOF \downarrow	Training time per iter. (s)
2	16.90	0.571	0.409	0.750	0.095
6	17.33	0.591	0.376	0.675	0.161
10	17.19	0.579	0.383	0.675	0.226

F Limitation and Future Work

In the Blurry iPhone dataset, there is one continuous training monocular video for each scene. Additionally, two fixed cameras with novel views are provided for evaluation, following the evaluation protocol of the original iPhone dataset [19]. This configuration makes it challenging to train deep-learning-based methods on unseen information that may be requested for evaluation. For instance, in some specific scenes, as shown in Fig. 12, due to different lighting environments, the tone of validation views can only be observed in a significantly small number of training samples (View 2). Hence, all kinds of radiance fields are generally overfitted to the major lighting condition of View 1. This challenge arises from the dataset’s characteristics, which exhibit extremely diverse training and validation views. Introduction of relighting technique, modeling of reflectance component or balancing training data can be one of an option to handle this issue and we leave it for one of our future work.

On the other hand, the emergence of concurrent work on Gaussian Splatting-based dynamic methods, such as in 4D-GS [62], brings improved training and rendering efficiencies. However, according to our current experiments of Tab. 1, Tab. 4 and the demo video, 4D-GS [62] struggles with handling highly monocular videos, as seen in our Blurry iPhone dataset and the original iPhone dataset [19]. Therefore, we plan to enhance our framework by integrating the Gaussian Splatting shading network into our effective motion-aware deblurring strategy for our future work.

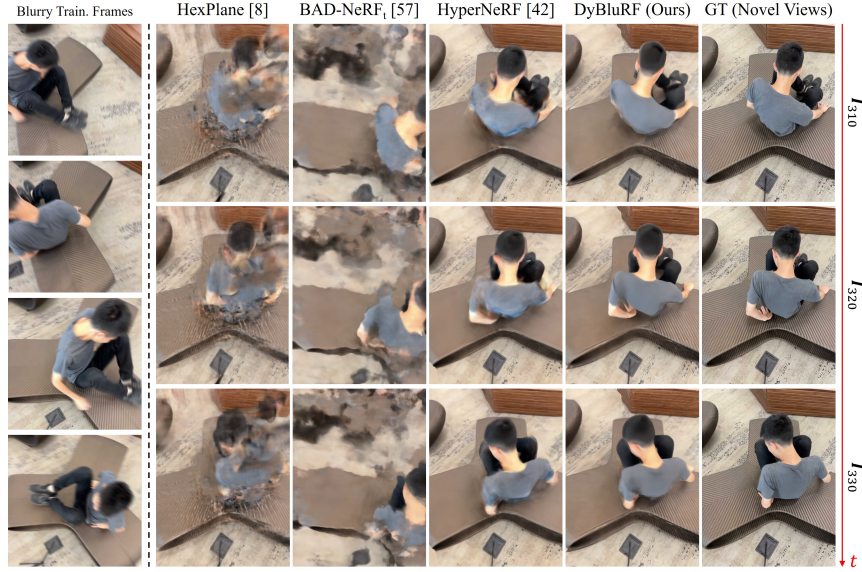


Fig. 13: Dynamic deblurring novel view synthesis results. We compare the novel view synthesis quality of our DyBluRF for *Spin* scene with the existing methods [8, 24, 42]. Each row corresponds to the 310th, 320th and 330th frame, respectively.



Fig. 14: Dynamic deblurring novel view synthesis results. We compare the novel view synthesis quality of our DyBluRF for *Paper-windmill* scene with the existing methods [8, 24, 42]. Each row corresponds to the 198th, 203th and 208th frame, respectively.

References

1. Roboflow, <https://roboflow.com/> 14
2. Argaw, D.M., Kim, J., Rameau, F., Zhang, C., Kweon, I.S.: Restoration of video frames from a single blurred image with motion understanding. In: Proceedings of the IEEE/CVF Conference on Computer Vision and Pattern Recognition. pp. 701–710 (2021) 10, 17
3. Athar, S., Xu, Z., Sunkavalli, K., Shechtman, E., Shu, Z.: Rignerf: Fully controllable neural 3d portraits. In: CVPR (2022) 3
4. Attal, B., Huang, J.B., Richardt, C., Zollhoefer, M., Kopf, J., O’Toole, M., Kim, C.: Hyperreel: High-fidelity 6-dof video with ray-conditioned sampling. In: CVPR. pp. 16610–16620 (2023) 2, 4
5. Bahat, Y., Efrat, N., Irani, M.: Non-uniform blind deblurring by reblurring. In: ICCV. pp. 3286–3294 (2017) 2, 3
6. Bojanowski, P., Joulin, A., Lopez-Paz, D., Szlam, A.: Optimizing the latent space of generative networks. In: Proceedings of the 35th International Conference on Machine Learning, ICML 2018, Stockholm, Sweden, July 10–15, 2018 (2018) 5
7. Broxton, M., Flynn, J., Overbeck, R., Erickson, D., Hedman, P., Duvall, M., Dourgarian, J., Busch, J., Whalen, M., Debevec, P.: Immersive light field video with a layered mesh representation. *ACM Transactions on Graphics (TOG)* **39**(4), 86–1 (2020) 2
8. Cao, A., Johnson, J.: Hexplane: A fast representation for dynamic scenes. In: CVPR. pp. 130–141 (2023) 2, 4, 5, 10, 11, 17, 23, 24, 30
9. Chen, A., Xu, Z., Geiger, A., Yu, J., Su, H.: Tensorf: Tensorial radiance fields. In: ECCV. pp. 333–350. Springer (2022) 3
10. Chu, M., Xie, Y., Mayer, J., Leal-Taixé, L., Thuerey, N.: Learning temporal coherence via self-supervision for gan-based video generation. *ACM Transactions on Graphics (TOG)* **39**(4), 75–1 (2020) 10
11. Collet, A., Chuang, M., Sweeney, P., Gillett, D., Evseev, D., Calabrese, D., Hoppe, H., Kirk, A., Sullivan, S.: High-quality streamable free-viewpoint video. *ACM Transactions on Graphics (ToG)* **34**(4), 1–13 (2015) 2
12. Deng, S., Ren, W., Yan, Y., Wang, T., Song, F., Cao, X.: Multi-scale separable network for ultra-high-definition video deblurring. In: ICCV. pp. 14030–14039 (2021) 3
13. Drebin, R.A., Carpenter, L., Hanrahan, P.: Volume rendering. *ACM Siggraph Computer Graphics* **22**(4), 65–74 (1988) 3, 5
14. Du, Y., Zhang, Y., Yu, H.X., Tenenbaum, J.B., Wu, J.: Neural radiance flow for 4d view synthesis and video processing. In: ICCV. pp. 14304–14314. IEEE Computer Society (2021) 4
15. Fang, J., Yi, T., Wang, X., Xie, L., Zhang, X., Liu, W., Nießner, M., Tian, Q.: Fast dynamic radiance fields with time-aware neural voxels. In: SIGGRAPH Asia 2022 Conference Papers. pp. 1–9 (2022) 2, 3, 4, 5, 10, 11, 17, 24
16. Fridovich-Keil, S., Meanti, G., Warburg, F.R., Recht, B., Kanazawa, A.: K-planes: Explicit radiance fields in space, time, and appearance. In: CVPR. pp. 12479–12488 (2023) 2, 4
17. Fridovich-Keil, S., Yu, A., Tancik, M., Chen, Q., Recht, B., Kanazawa, A.: Plenoxels: Radiance fields without neural networks. In: CVPR. pp. 5501–5510 (2022) 3
18. Gao, C., Saraf, A., Kopf, J., Huang, J.B.: Dynamic view synthesis from dynamic monocular video. In: ICCV. pp. 5712–5721 (2021) 2, 3, 4, 5, 6, 9, 13, 25

19. Gao, H., Li, R., Tulsiani, S., Russell, B., Kanazawa, A.: Dynamic novel-view synthesis: A reality check. In: NeurIPS (2022) [2](#), [3](#), [4](#), [10](#), [11](#), [12](#), [17](#), [18](#), [19](#), [20](#), [21](#), [22](#), [23](#), [24](#), [26](#), [27](#), [29](#)
20. Gupta, A., Joshi, N., Zitnick, C.L., Cohen, M., Curless, B.: Single image deblurring using motion density functions. In: ECCV. pp. 171–184. Springer (2010) [2](#), [3](#)
21. Harmeling, S., Michael, H., Schölkopf, B.: Space-variant single-image blind deconvolution for removing camera shake. NeurIPS **23**, 829–837 (2010) [2](#), [3](#)
22. Jiang, W., Yi, K.M., Samei, G., Tuzel, O., Ranjan, A.: Neuman: Neural human radiance field from a single video. In: ECCV (2022) [3](#)
23. Kwak, J.g., Dong, E., Jin, Y., Ko, H., Mahajan, S., Yi, K.M.: Vivid-1-to-3: Novel view synthesis with video diffusion models. arXiv preprint arXiv:2312.01305 (2023) [10](#), [17](#)
24. Lee, D., Lee, M., Shin, C., Lee, S.: Dp-nerf: Deblurred neural radiance field with physical scene priors. In: CVPR. pp. 12386–12396 (2023) [2](#), [3](#), [4](#), [5](#), [6](#), [7](#), [10](#), [11](#), [12](#), [17](#), [22](#), [23](#), [24](#), [30](#)
25. Lee, D., Oh, J., Rim, J., Cho, S., Lee, K.M.: Exblurf: Efficient radiance fields for extreme motion blurred images. In: ICCV. pp. 17639–17648 (2023) [2](#), [3](#), [5](#)
26. Li, D., Shi, X., Zhang, Y., Cheung, K.C., See, S., Wang, X., Qin, H., Li, H.: A simple baseline for video restoration with grouped spatial-temporal shift. In: Proceedings of the IEEE/CVF Conference on Computer Vision and Pattern Recognition. pp. 9822–9832 (2023) [2](#), [3](#), [10](#), [11](#), [12](#), [14](#), [24](#)
27. Li, T., Slavcheva, M., Zollhoefer, M., Green, S., Lassner, C., Kim, C., Schmidt, T., Lovegrove, S., Goesele, M., Newcombe, R., Lv, Z.: Neural 3d video synthesis from multi-view video. In: CVPR. pp. 5521–5531 (2022) [2](#), [4](#), [6](#)
28. Li, Z., Niklaus, S., Snavely, N., Wang, O.: Neural scene flow fields for space-time view synthesis of dynamic scenes. In: CVPR. pp. 6498–6508 (2021) [2](#), [3](#), [4](#), [5](#), [9](#), [12](#), [13](#), [19](#), [22](#)
29. Li, Z., Wang, Q., Cole, F., Tucker, R., Snavely, N.: Dynibar: Neural dynamic image-based rendering. In: CVPR. pp. 4273–4284 (2023) [2](#), [3](#), [4](#), [5](#), [6](#), [9](#)
30. Liang, J., Fan, Y., Xiang, X., Ranjan, R., Ilg, E., Green, S., Cao, J., Zhang, K., Timofte, R., Van Gool, L.: Recurrent video restoration transformer with guided deformable attention. In: NeurIPS (2022) [3](#)
31. Liu, Y., Gao, C., Meuleman, A., Tseng, H., Saraf, A., Kim, C., Chuang, Y., Kopf, J., Huang, J.: Robust dynamic radiance fields. In: CVPR. pp. 13–23 (2023) [3](#), [5](#), [9](#), [13](#), [14](#), [19](#), [22](#), [24](#), [25](#)
32. Ma, L., Li, X., Liao, J., Zhang, Q., Wang, X., Wang, J., Sander, P.V.: Deblur-nerf: Neural radiance fields from blurry images. In: CVPR. pp. 12861–12870 (2022) [2](#), [3](#), [4](#), [5](#), [6](#)
33. Mildenhall, B., Srinivasan, P.P., Tancik, M., Barron, J.T., Ramamoorthi, R., Ng, R.: Nerf: Representing scenes as neural radiance fields for view synthesis. In: ECCV (2020) [2](#), [3](#), [5](#), [17](#), [22](#)
34. Nah, S., Baik, S., Hong, S., Moon, G., Son, S., Timofte, R., Lee, K.M.: Ntire 2019 challenge on video deblurring and super-resolution: Dataset and study. In: CVPR Workshops (June 2019) [6](#), [10](#)
35. Nah, S., Hyun Kim, T., Mu Lee, K.: Deep multi-scale convolutional neural network for dynamic scene deblurring. In: Proceedings of the IEEE conference on computer vision and pattern recognition. pp. 3883–3891 (2017) [6](#), [10](#)
36. Oh, J., Kim, M.: Demfi: deep joint deblurring and multi-frame interpolation with flow-guided attentive correlation and recursive boosting. In: ECCV. pp. 198–215. Springer (2022) [2](#), [3](#), [6](#)

37. Oswald, M.R., Stühmer, J., Cremers, D.: Generalized connectivity constraints for spatio-temporal 3d reconstruction. In: ECCV. pp. 32–46. Springer (2014) [2](#)
38. Pan, J., Bai, H., Tang, J.: Cascaded deep video deblurring using temporal sharpness prior. In: CVPR. pp. 3043–3051 (2020) [3](#)
39. Pan, J., Sun, D., Pfister, H., Yang, M.H.: Blind image deblurring using dark channel prior. In: CVPR. pp. 1628–1636 (2016) [2](#), [3](#)
40. Pan, J., Xu, B., Dong, J., Ge, J., Tang, J.: Deep discriminative spatial and temporal network for efficient video deblurring. In: CVPR. pp. 22191–22200 (2023) [2](#)
41. Park, K., Sinha, U., Barron, J.T., Bouaziz, S., Goldman, D.B., Seitz, S.M., Martin-Brualla, R.: Nerfies: Deformable neural radiance fields. In: ICCV. pp. 5865–5874 (2021) [3](#), [7](#)
42. Park, K., Sinha, U., Hedman, P., Barron, J.T., Bouaziz, S., Goldman, D.B., Martin-Brualla, R., Seitz, S.M.: Hypernerf: A higher-dimensional representation for topologically varying neural radiance fields. ACM Trans. Graph. **40**(6) (dec 2021) [2](#), [3](#), [4](#), [5](#), [10](#), [11](#), [12](#), [17](#), [19](#), [21](#), [22](#), [24](#), [30](#)
43. Park, S., Son, M., Jang, S., Ahn, Y.C., Kim, J.Y., Kang, N.: Temporal interpolation is all you need for dynamic neural radiance fields. In: CVPR. pp. 4212–4221 (2023) [2](#)
44. Píala, M., Clark, R.: Terminerf: Ray termination prediction for efficient neural rendering. In: 3DV. pp. 1106–1114 (2021) [8](#)
45. Pumarola, A., Corona, E., Pons-Moll, G., Moreno-Noguer, F.: D-nerf: Neural radiance fields for dynamic scenes. In: CVPR. pp. 10318–10327 (2021) [2](#), [3](#)
46. Ranftl, R., Bochkovskiy, A., Koltun, V.: Vision transformers for dense prediction. In: ICCV. pp. 12159–12168 (2021) [9](#)
47. Schonberger, J.L., Frahm, J.M.: Structure-from-motion revisited. In: CVPR. pp. 4104–4113 (2016) [5](#)
48. Shao, R., Zheng, Z., Tu, H., Liu, B., Zhang, H., Liu, Y.: Tensor4d: Efficient neural 4d decomposition for high-fidelity dynamic reconstruction and rendering. In: CVPR. pp. 16632–16642 (2023) [2](#), [4](#)
49. Shen, W., Bao, W., Zhai, G., Chen, L., Min, X., Gao, Z.: Blurry video frame interpolation. In: CVPR. pp. 5114–5123 (2020) [6](#)
50. Sim, H., Oh, J., Kim, M.: Xvfi: extreme video frame interpolation. In: ICCV. pp. 14489–14498 (2021) [10](#), [17](#), [18](#)
51. Song, L., Chen, A., Li, Z., Chen, Z., Chen, L., Yuan, J., Xu, Y., Geiger, A.: Nerf-player: A streamable dynamic scene representation with decomposed neural radiance fields. IEEE Transactions on Visualization and Computer Graphics **29**(5), 2732–2742 (2023) [3](#)
52. Teed, Z., Deng, J.: Raft: Recurrent all-pairs field transforms for optical flow. In: ECCV. pp. 402–419. Springer (2020) [9](#), [13](#), [14](#)
53. Telleen, J., Sullivan, A., Yee, J., Wang, O., Gunawardane, P., Collins, I., Davis, J.: Synthetic shutter speed imaging. In: Computer Graphics Forum. pp. 591–598. Wiley Online Library (2007) [2](#), [3](#)
54. Tretschk, E., Tewari, A., Golyanik, V., Zollhöfer, M., Lassner, C., Theobalt, C.: Non-rigid neural radiance fields: Reconstruction and novel view synthesis of a dynamic scene from monocular video. In: ICCV. pp. 12959–12970 (2021) [2](#), [3](#)
55. Van Hoorick, B., Tendulkar, P., Suris, D., Park, D., Stent, S., Vondrick, C.: Revealing occlusions with 4d neural fields. In: CVPR. pp. 3011–3021 (2022) [4](#)
56. Wang, L., Zhang, J., Liu, X., Zhao, F., Zhang, Y., Zhang, Y., Wu, M., Yu, J., Xu, L.: Fourier plenotrees for dynamic radiance field rendering in real-time. In: CVPR. pp. 13524–13534 (2022) [2](#)

57. Wang, P., Zhao, L., Ma, R., Liu, P.: Bad-nerf: Bundle adjusted deblur neural radiance fields. In: CVPR. pp. 4170–4179 (2023) [2](#), [3](#), [4](#), [5](#), [6](#), [10](#), [11](#), [12](#), [17](#), [22](#), [23](#), [24](#)
58. Wang, Y., Lu, Y., Gao, Y., Wang, L., Zhong, Z., Zheng, Y., Yamashita, A.: Efficient video deblurring guided by motion magnitude. In: ECCV (2022) [3](#)
59. Wang, Z., Wu, S., Xie, W., Chen, M., Prisacariu, V.A.: Nerf-: Neural radiance fields without known camera parameters. CoRR (2021) [12](#)
60. Weng, C.Y., Curless, B., Srinivasan, P.P., Barron, J.T., Kemelmacher-Shlizerman, I.: Humannerf: Free-viewpoint rendering of moving people from monocular video. In: CVPR. pp. 16210–16220 (2022) [2](#)
61. Weng, C.Y., Curless, B., Srinivasan, P.P., Barron, J.T., Kemelmacher-Shlizerman, I.: HumanNeRF: Free-viewpoint rendering of moving people from monocular video. In: CVPR. pp. 16210–16220 (June 2022) [3](#)
62. Wu, G., Yi, T., Fang, J., Xie, L., Zhang, X., Wei, W., Liu, W., Tian, Q., Wang, X.: 4d gaussian splatting for real-time dynamic scene rendering. In: CVPR (2024) [2](#), [4](#), [5](#), [10](#), [11](#), [12](#), [19](#), [22](#), [24](#), [29](#)
63. Xian, W., Huang, J.B., Kopf, J., Kim, C.: Space-time neural irradiance fields for free-viewpoint video. In: CVPR. pp. 9421–9431 (2021) [4](#)
64. Yan, Z., Li, C., Lee, G.H.: Nerf-ds: Neural radiance fields for dynamic specular objects. In: CVPR (2023) [9](#)
65. Yang, G., Vo, M., Natalia, N., Ramanan, D., Andrea, V., Hanbyul, J.: Banmo: Building animatable 3d neural models from many casual videos. In: CVPR (2022) [3](#)
66. Zhang, H., Xie, H., Yao, H.: Spatio-temporal deformable attention network for video deblurring. In: ECCV (2022) [3](#)
67. Zhang, K., Luo, W., Zhong, Y., Ma, L., Liu, W., Li, H.: Adversarial spatio-temporal learning for video deblurring. IEEE Transactions on Image Processing **28**(1), 291–301 (2018) [2](#), [3](#)
68. Zhang, K., Luo, W., Zhong, Y., Ma, L., Stenger, B., Liu, W., Li, H.: Deblurring by realistic blurring. In: CVPR. pp. 2737–2746 (2020) [2](#), [3](#)
69. Zhang, L., Curless, B., Seitz, S.M.: Spacetime stereo: Shape recovery for dynamic scenes. In: CVPR. vol. 2, pp. II–367. IEEE (2003) [2](#)
70. Zhang, Z., Cole, F., Tucker, R., Freeman, W.T., Dekel, T.: Consistent depth of moving objects in video. ACM Transactions on Graphics (TOG) (2021) [9](#)
71. Zhou, S., Zhang, J., Pan, J., Xie, H., Zuo, W., Ren, J.: Spatio-temporal filter adaptive network for video deblurring. In: ICCV. pp. 2482–2491 (2019) [3](#)
72. Zhu, Q., Zhou, M., Zheng, N., Li, C., Huang, J., Zhao, F.: Exploring temporal frequency spectrum in deep video deblurring. In: ICCV. pp. 12428–12437 (2023) [2](#)
73. Zitnick, C.L., Kang, S.B., Uyttendaele, M., Winder, S., Szeliski, R.: High-quality video view interpolation using a layered representation. ACM transactions on graphics (TOG) **23**(3), 600–608 (2004) [2](#)